Transport and dispersion of particles in visco-plastic fluids

by

Sarah Hormozi

B.Sc. Mechanical Engineering, Shiraz University, 2003
M.Sc. Mechanical Engineering, Sharif University of Technology, 2006
Ph.D. Mechanical Engineering, The University of British Columbia, 2011

A THESIS SUBMITTED IN PARTIAL FULFILLMENT OF
THE REQUIREMENTS FOR THE DEGREE OF

MASTER OF SCIENCE

in

The Faculty of Graduate and Postdoctoral Studies

(Mathematics)

THE UNIVERSITY OF BRITISH COLUMBIA

(Vancouver)

August 2013

Abstract

This thesis focuses on development of a model to predict "spreading" of the solids (i.e. proppant) fraction during the fracturing operation. We develop a 1D model that allows us to estimate dispersion of solid particles along a vertical pipe in a fully turbulent flow of a shear thinning yield stress fluid (i.e., visco-plastic fluid), as well as slip relative to the mean flow. In dimensionless form, this results in a quasilinear advection-diffusion equation. Advection by the mean flow, particle settling relative to the mean, in the direction of gravity, turbulent particle dispersivity and Taylor dispersion are the 4 main transport phenomena modelled in the 1D model. We provide a simple analysis of the 1D model, suitable for spreadsheet-type field design purposes, in which we estimate "mixing lengths" due to both settling and dispersion. Secondly, we provide an accurate numerical algorithm for solution of the 1D model and show how pulses of proppant (i.e. slugs) may or may not interact for typical process parameters.

Preface

The author of this thesis was the principal contributor to this research. Professor Ian Frigaard supervised the research.

Table of Contents

List of Tables

List of Figures

Acknowledgments

I would like to express my sincere gratitude and appreciation to those who assisted me during the course of this program.

Professor Ian Frigaard for serving as my advisor since 2008. Ian gave me the opportunity to work in several different areas of fluid mechanics ranging from hard core computations to lab-scale experiments to applied mathematical techniques. Ian showed me the beauty of Mathematics through his insightful scientific guidance. This inspired me to persue my education in Mathematics to bridge science and engineering. Ian's constant support and amiable personality have been of great value to me. I was truly blessed to be his student during the best school years of my life at UBC.

Dr Dmitry Eskin for his useful advice on this research.

Professor Neil Balmforth, Professor Michael Ward and Professor George Bluman for their supervision, advice, and guidance on some other research directions. Additionally, I was fortunate to take few Applied Mathematics courses from these gifted teachers.

Professor Bud Homsy for his guidance and support throughout, for keeping an open door, for helpful advice on presentation and for shared physical insight.

My friends in UBC and elsewhere, for their company and friendship. In particular, Dr Ali Vakil, Dr Mona Rahmani, Dr Anirban Guha, Professor Bahman Gharesifard and Mahtab Fathinejad for their continuous support.

My close family and my husband, Hamed, who stood by me and supported all my ideas and dreams. I love you dearly.

Finally, financial support of Schlumberger is gratefully acknowledged.

Dedication

To my family and friends.

Chapter 1

Introduction

It is common that many oil and gas wells do not produce at the expected rate. Hydraulic fracturing is a stimulation technique used to increase the productivity of wells in oil and gas reservoirs. In hydraulic fracturing, specially engineered suspensions are pumped at high pressure and rate into the reservoir, causing a propagating fracture to open. When the pressure is released the fracture is supported by the grains of solid (called proppant) that are left behind (see Fig.1.1). The increase in productivity results because the hydraulic conductivity of the fracture, filled with proppant, is significantly higher than that of the surrounding formation. More details on hydraulic fracturing can be found in [46].

A recent trend in the oil industry is to use the cyclic pumping of a proppant slurry interspersed with clear fracking fluid. This procedure is found to increase the subsequent productivity (see e.g., [11, 39, 40]), over that due to conventional fracturing with a continuous stream of propant. It is therefore of interest to understand how slugs of proppant pumped in a cyclic fashion can disperse, both in the pipe on the way to the fracture and within the fracture itself. More clearly, under which physical situations do slugs of proppant interfere with one another or remain distinct.

1.1 Objectives of the thesis

The overall objective of this thesis is to develop models to predict "spreading" of the solids (i.e. proppant) fraction during the fracturing operation. In particular, we focus at transport of proppant along a vertical uniform pipe

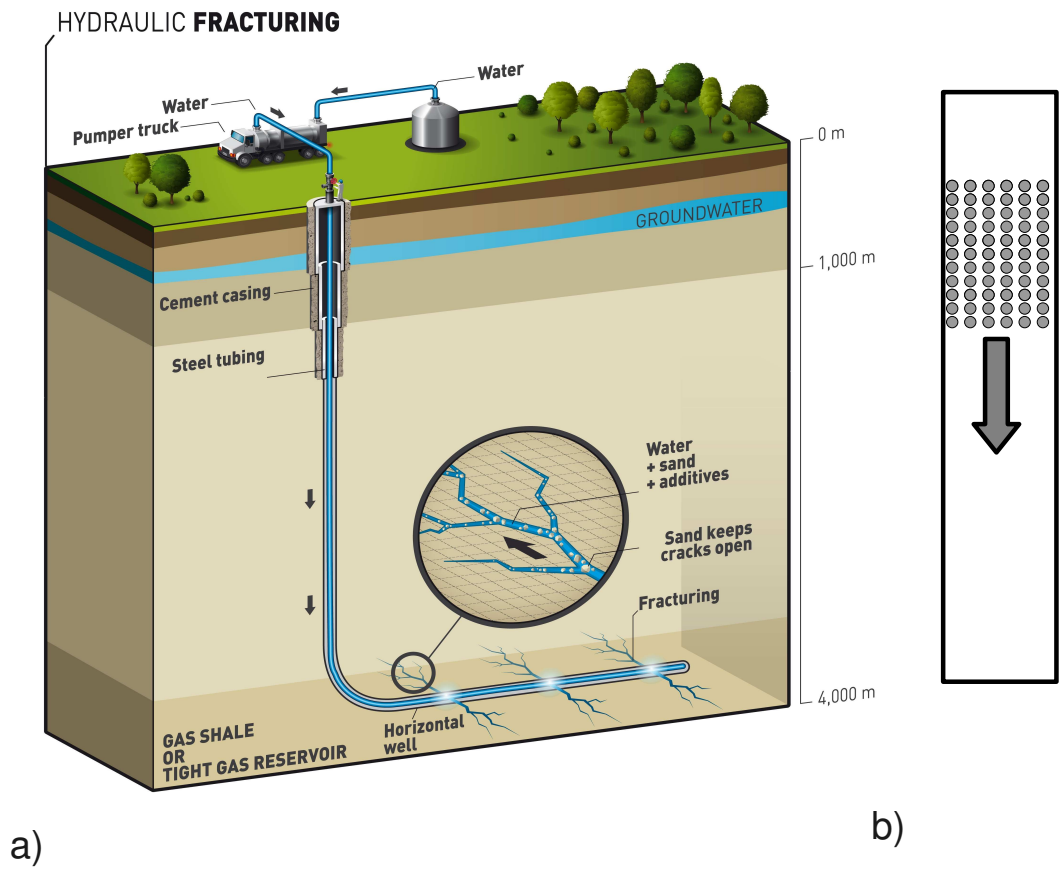

Figure 1.1: a) Schematic of hydraulic fracturing from *http://en.skifergas.dk/*; b) Particulate fluid cycle in the pipe/wellbore.

(simulating transport to the fracture). We first examine typical flow regimes over a range of process parameters, in order to characterize the transport phenomena that are likely to be dominant. Next we develop a 1D model that allows us to estimate: (i) dispersion of solid particles along a vertical pipe in a fully turbulent flow of a shear thinning yield stress fluid, and (ii) slip of the solid phase relative to the mean flow. In dimensionless form, we end up with

the following advection-diffusion equation:

$$\frac{\partial \bar{\phi}}{\partial t} + \frac{\partial F}{\partial z} = \frac{\partial}{\partial z}[D\frac{\partial \bar{\phi}}{\partial z}]. \tag{1.1}$$

In this equation $\bar{\phi}(z,t)$ represents the average concentration of solids, z is a dimensionless length, scaled with the pipe length $\hat{L}$ and t is dimensionless time, scaled with $\hat{L}/\hat{U}_0$, where $\hat{U}_0$ is the mean axial velocity. The function F includes the averaged effect of settling relative to the mean flow, and D represents the total diffusivity/disspersivity of the flow. As well as deriving (1.1), we give analytical estimates for both the advective and diffusive contributions to the spreading of solids. Finally, we implement a robust numerical scheme for solving (1.1), which allows us to investigate various pumping strategies.

1.2 Literature overview

In general, models of fracturing hydraulics have focused on the fracture itself. Models range from simplified hydraulic descriptions to those that consider two-phase governing equations, assuming that solid (proppant) and fluid phases can be described as two phases of incompressible continua. Here, we review only models of the fracturing flows in the pipe/wellbore.

The majority of fracturing flows within the wellbore are highly turbulent due to the high flow rates and relatively small pipe diameters [1] Thus, frequently these are considered as fully homogeneous mixtures. In the case that the flow rates are moderate/low and the fracking fluid rheology is high, the particle-scale flows are non-inertial and appropriate models would consider the mixture as a (non-Newtonian) viscous suspension. For higher flow rates and lower viscosities, viscous effects are less important on the particle scale and the two phases must be considered separately.

[1] Here, we assume that the fracturing fluid is shear thinning. Therefore, shear rate increases with decreasing the pipe diameters. This gives smaller viscosity and consequently higher Reynolds number see (1.6).

Models for pipe flow of homogeneous Newtonian suspension abound, in particular being developed for the mining industry, e.g. [35, 37]. These are often however focused at critical velocities and the onset of beds in near-horizontal pipelines. For vertical pipes, the solids distribution across the pipe may be assumed to be fairly uniform, so that a 1D hydraulic approach makes sense.

Our focus is however on dispersion of proppant slugs along the pipe. If the suspension is really treated as a single fluid mixture, then this logically leads to descriptions of the particle diffusivity that are similar to those for the liquid phase. There are some developments of this idea based on dimensional analysis coupled to data-fitting, e.g. [48]. The main point to note however is that, as with turbulent flow of liquids, the dominant process in spreading the solid particles axially is dispersion by the axial velocity field.

Although there is considerable work on modelling of Newtonian suspensions, i.e. those in which the liquid carrier phase is Newtonian, there is less on non-Newtonian suspensions. This understanding is however evolving rapidly. At the level of continuum modelling of suspension rheology, perhaps the most comprehensive studies that concern yield stress fluids have been carried out by Ovarlez and co-workers, [3, 5, 26, 31, 32, 47], who have used a mix of experimental and modelling techniques in developing a general framework that has been validated in some limits. We will adopt a rheological model that fits with this general framework.

For more inertial suspension flows (on a particle scale) we are still in the situation that the dominant spreading mechanism will be through axial dispersion, but the particle diffusivity becomes distinct from that of the liquid phase. Eskin and co-workers have developed a "Kolmogoroff approach" to slurry pipeline flows; see [14, 15]. This approach assumes the spectral energy density distribution of eddies, but modifies the range of the spectrum according to particle size/separation considerations. Essentially the small scale cut-off is increased by the presence of particles. It is considered that eddies with size

below this cut-off transform their energy into small-scale chaotic motions of particles. Eskin [14] shows that the neglect of this part of the spectrum has only a minimal effect on the rms eddy velocity scale. In [15] the fraction of energy dissipated in solid-liquid interactions is estimated and is used to modify the solids phase diffusivity.

More recently, a simpler semi-empirical approach has been adopted [17], that resembles that of [48] in coupling dimensional analysis to data-fitting. This leads to a relatively simple expression for the solids diffusivity that includes the effects of particle diameter ratio, δ_p.

1.3 Dimensional analysis

We aim to model the flow of a proppant-laden shear thinning fracturing fluid, possibly with yield stress, that is being pumped in turbulent flow downward along a (vertical) pipe. The flow described will depend on at least the following set of physical parameters.

- The pipe diameter, $\hat{D}$.
- The pipe length, $\hat{L}$.
- A representative particle diameter for the proppant (solids phase), $\hat{d}_p$.
- The liquid phase density, $\hat{\rho}_f$.
- The solids phase density, $\hat{\rho}_s$.
- Gravitational acceleration, $\hat{g}$.
- The flow rate of the slurry, $\hat{Q}$, measured positive in the downwards direction along the pipe.
- The yield stress of the particle free fluid, $\hat{\tau}_{Y0}$.
- The consistency coefficient of the particle free fluid, $\hat{K}_0$.

- The power law index of the particle free fluid, n.
- The volume fraction of solid phase, ϕ.

The last two parameters are dimensionless. The first 9 parameters depend on a 3 independent dimensions. Throughout this thesis we will adopt the practice of denoting all dimensional quantities by the $\hat{\cdot}$ symbol. Thus, the flow is minimally described by 6 dimensionless groups, plus the volume fraction of proppant (solid phase) ϕ, and the power law index n. We will adopt the following 6 principal dimensionless groups

$$s = \frac{\hat{\rho}_s}{\hat{\rho}_f} = \text{Density ratio}, \tag{1.2}$$

$$Fr = \sqrt{\frac{\hat{U}_0^2}{\hat{g}\hat{D}(s-1)}} = \text{Densimetric Froude number} = \frac{\text{Imposed velocity}}{\text{Buoyancy velocity}}, \tag{1.3}$$

$$\delta = \frac{\hat{D}}{\hat{L}} = \text{Aspect ratio of the pipe}, \tag{1.4}$$

$$\delta_p = \frac{\hat{d}_p}{\hat{D}} = \text{Particle to pipe diameter ratio}, \tag{1.5}$$

$$Re = \frac{\hat{\rho}_f \hat{U}_0^2}{\hat{K}_0(\hat{U}/(\hat{D}/2))^n} = \text{Reynolds number} = \frac{\text{Inertial stresses}}{\text{Viscous stresses}}, \tag{1.6}$$

$$B = \frac{\hat{\tau}_{Y0}}{\hat{K}_0(\hat{U}_0/(\hat{D}/2))^n} = \text{Bingham number} = \frac{\text{Yield stress}}{\text{Viscous stress in the flow}}. \tag{1.7}$$

Where $\hat{U}_0 = 4\hat{Q}/(\pi\hat{D}^2)$ is the mean velocity. In describing different physical phenomena and closure models, it is often convenient to use other variables, which we will do. However, these other groups may be expressed algebraically as functions of the above.

Table 1.1 and Table 1.2 show the ranges of dimensional and non-dimensional parameters respectively that we consider representative of the industrial application. The base set of parameters leading to the above dimensionless groups is

Industrial Data		
Parameter	Unit	Range
$\hat{D}$	(mm)	$50 - 120$
$\hat{L}$	(m)	$500 - 3000$
$\hat{d}_p$	(mm)	$0.1 - 2$
$\hat{\rho}_f$	(kg/m^3)	1000
$\hat{\rho}_s$	(kg/m^3)	$2650 - 3650$
$\hat{U}_0$	(m/s)	$2 - 25$
$\hat{\tau}_{Y0}$	(Pa)	$0 - 10$
$\hat{K}_0$	$(Pa.s^n)$	$0.01 - 5.0$
n	-	$0.2 - 1$
ϕ	-	$5\% - 40\%$

Table 1.1: Typical ranges of the dimensional process parameters in the industrial application.

Dimensionless parameters	Range
s	$2.65 - 3.65$
Fr	$1.1 - 27.8$
δ	$10^{-4} - 10^{-3}$
δ_p	$0.0008 - 0.04$
Re	$3 \times 10^3 - 10^7$
B	$0 - 100$

Table 1.2: The range of non-dimensional parameters in the industrial application.

clearly not sufficient to fully describe all phenomena one is likely to encounter in a pipe flow of a turbulent suspension. Characterizing the particle distribution via a single parameter is a gross simplification, (but perhaps necessary), apart from a size distribution of particles other mechanical and geometric parameters may become important, e.g. friction coefficient, maximal packing fraction, wall roughness etc...

Based on the ranges of physical parameters likely to be encountered, we may begin to characterise the flow along the pipe, into the well. This characterisation has been performed in [18], considering both the bulk flow and particle scale effects. The first conclusion is that the bulk flow of most fracturing flows when traveling down the well is a fully turbulent suspension flow. Apart from depletion layers close to the pipe walls we can expect turbulent eddies to make the leading order solids concentration uniform across the pipe. Only in more extreme cases of low flow rates and very viscous fracturing fluids would we begin to enter a weakly turbulent or laminar regime, which would result in increased dispersion relative to the mean flow. Secondly, on the particle scale it was found that flows range from those where particle dynamics are essentially Stokesian (low to moderate flow rates and moderate fracking fluid rheologies) through to those where the particle dynamics may be inertial and the interphase coupling relatively weak. The latter results from a combination of low rheology and high shear rates.

Some idea of the range of sedimentation velocities can be gained from application of classical correlations for hindered settling, e.g. Richardson and Zaki [36], assuming the typical ranges for the effective viscosity given in Table 1.1. We can show that the particle settling velocity, $\hat{v}_p$, is typically less than $10^{-3}\hat{U}_0$. The ratio between particle settling and bulk velocities indicates the distance settled during transit along the pipe, compared to the length of pipe. While this distance can be of the order of $1-3m$ it is important to note that an entire slug of proppant would be settling at similar rates. Insofar as dispersion of a slug is concerned, advective dispersion is governed by the difference in particle velocity as ϕ ranges over $[0, \phi_{in}]$. Taking a typical $\phi_{in} \approx 0.3$, typically $\hat{v}_p$ could range from $\hat{v}_{p0}$ to $0.25\hat{v}_{p0}$, meaning that the dispersive effect is comparable to the net settling effect. Here $\hat{v}_{p0}$ represents the unhindered settling velocity. Therefore, it would be unwise to neglect particle settling even in vertical pipes. Although we expect that other effects will be dominant, it is conceivable that with shorter time intervals between pulsed slugs and for

long wells, settling due to advection could become relevant. Note also that advective spreading is linear in transit time ($\hat{t}_{transit} = \hat{L}/\hat{U}_0$), whereas diffusive spreading should increase like $\hat{t}_{transit}^{1/2}$.

1.4 Outline of the thesis

In chapter 2, we derive a model for particle transport, reduce the model via physical scaling arguments and finally use the method of multiple-scale to derive a 1D advection-diffusion model for transport and dispersion of the mean solid particle concentration along the wellbore. The advection part of the model includes the transport of the solid phase with the mean flow velocity and the mean particle settling velocity. The diffusion part of the model includes both the averaged turbulent particle diffusivity and the effect of Taylor dispersion. In chapter 3, we develop a robust numerical algorithm to solve the nonlinear 1D advection/diffusion model. This algorithm is used to study the spreading of the slug of solid along the well for few industrial examples. The thesis concludes in chapter 4 with a summary and number of general recommendations.

Chapter 2

Modeling approach

The overall objective of this chapter is to derive a 1D advection diffusion equation (1.1) to estimate dispersion of solid particles along a vertical pipe in a fully turbulent flow of a shear thinning yield stress fluid. The advection part of the model includes the transport of the solid phase with the mean flow velocity and the mean particle settling velocity. The diffusion part of the model includes both the averaged turbulent particle diffusivity and the effect of Taylor dispersion. We also provide a simple analysis of (1.1), suitable for spreadsheet-type field design purposes, in which we estimate "mixing lengths" due to to both settling and dispersion.

2.1 Formulation

We start with the governing equations for two incompressible continuous phases. Then, we derive the governing equations for the mixture and explain the transport equation for the dispersed phase. We explain the constitutive law for the mixture and we obtain the averaged velocity profile for a fully developed turbulent flow of a shear thinning yield stress fluid in a pipe. Finally, we give the closures for the solid-fluid interaction force and relative velocity.

2.1.1 Mass conservation and particle diffusivity

We assume that solid and fluid phases can be described as two phases of incompressible continua, which implies some form volume-averaging over a scale larger than the particle scale in interpreting the flow variables. The mass

conservation equations for each phase are:

$$\hat{\rho}_s \frac{\partial \phi}{\partial \hat{t}} + \hat{\nabla} \cdot (\hat{\rho}_s \phi \hat{\mathbf{u}}_p) = 0, \tag{2.1}$$

$$\hat{\rho}_f \frac{\partial (1-\phi)}{\partial \hat{t}} + \hat{\nabla} \cdot (\hat{\rho}_f (1-\phi) \hat{\mathbf{u}}_f) = 0. \tag{2.2}$$

Where ϕ is the local volume fraction of solid. The phase-averaged solid and fluid velocities are denoted by $\hat{\mathbf{u}}_p$ and $\hat{\mathbf{u}}_f$ respectively. On dividing through (2.1) by $\hat{\rho}_s$ and (2.2) by $\hat{\rho}_f$, then summing:

$$\hat{\nabla} \cdot \hat{\mathbf{u}} = 0 : \qquad \hat{\mathbf{u}} = \phi \hat{\mathbf{u}}_p + (1-\phi) \hat{\mathbf{u}}_f. \tag{2.3}$$

Here $\hat{\mathbf{u}}$ is the volume-averaged velocity for the mixture of solid and fluid phases. Equation (2.1) can be rewritten, in terms of $\hat{\mathbf{u}}$ and the relative velocity between solid and liquid phases:

$$\frac{\partial \phi}{\partial \hat{t}} + \hat{\nabla} \cdot [\phi \hat{\mathbf{u}} + \phi (1-\phi) \hat{\mathbf{u}}_r] = 0, \tag{2.4}$$

where $\hat{\mathbf{u}}_r = \hat{\mathbf{u}}_p - \hat{\mathbf{u}}_f$.

In practice, as we consider turbulent flows, we are more interested in the average behaviour of the flow variables, which may evolve temporally and spatially. Therefore, we consider ensemble-averaged quantities, denoted with an over-bar, and fluctuating components:

$$\phi = \bar{\phi} + \phi', \qquad \hat{\mathbf{u}}_p = \hat{\bar{\mathbf{u}}}_p + \hat{\mathbf{u}}'_p, , \qquad \hat{\mathbf{u}}_f = \hat{\bar{\mathbf{u}}}_f + \hat{\mathbf{u}}'_f, \quad \text{etc.}$$

Ensemble averaging of (2.4) leads to:

$$\frac{\partial \bar{\phi}}{\partial \hat{t}} + \hat{\nabla} \cdot [\bar{\phi} \hat{\bar{\mathbf{u}}} + \bar{\phi}(1-\bar{\phi}) \hat{\bar{\mathbf{u}}}_r] = \hat{\Gamma}_c, \tag{2.5}$$

where the term $\hat{\Gamma}_c$ results from correlation of the fluctuating components of

the velocity and solids fraction fields. More formally, we can identify $\hat{\Gamma}_c$:

$$\hat{\Gamma}_c = -\hat{\nabla} \cdot [\overline{\phi' \hat{\mathbf{u}}'} + (1 - 2\bar{\phi})\overline{\phi' \hat{\mathbf{u}}'_r} - \overline{(\phi')^2}\hat{\bar{\mathbf{u}}}_r] \approx -\hat{\nabla} \cdot [\overline{\phi' \hat{\mathbf{u}}'}], \tag{2.6}$$

on assuming that the relative velocity terms as relatively small. Typically now, the quantity $\hat{\Gamma}_c$ is modeled as a diffusive flux via Fick's law, in order to close the equations, i.e.

$$\overline{\phi' \hat{\mathbf{u}}'_p} = -\hat{D}_d \hat{\nabla} \bar{\phi}, \tag{2.7}$$

where $\hat{D}_d$ is the particle diffusivity coefficient. An expression for $\hat{D}_d$ has to be determined either from experiment or through some auxiliary analysis.

Finally, we ensemble-average (2.3) to give:

$$\hat{\nabla} \cdot \hat{\bar{\mathbf{u}}} = 0, \tag{2.8}$$

and the solids phase mass conservation approximation:

$$\frac{\partial \bar{\phi}}{\partial \hat{t}} + \hat{\nabla} \cdot [\bar{\phi}\hat{\bar{\mathbf{u}}} + \bar{\phi}(1 - \bar{\phi})\hat{\bar{\mathbf{u}}}_r] \quad = \quad \hat{\nabla} \cdot [\hat{D}_d \hat{\nabla} \bar{\phi}], \tag{2.9}$$

We note that (2.9) contains the main components necessary to model dispersion along the pipe. It is necessary to provide closure expressions for the mean axial velocity, the relative velocity and the particle diffusivity.

2.1.2 Momentum balance

The linear momentum balances for each phase can be written as:

$$\hat{\rho}_s \phi \left(\frac{\partial \hat{\mathbf{u}}_p}{\partial \hat{t}} + (\hat{\mathbf{u}}_p \cdot \hat{\nabla})\hat{\mathbf{u}}_p \right) \quad = \quad \hat{\nabla} \cdot \hat{\mathbf{\Sigma}}_p + \hat{\rho}_s \phi \hat{g} \boldsymbol{k} + \hat{\mathbf{m}}, \tag{2.10}$$

$$\hat{\rho}_f (1 - \phi) \left(\frac{\partial \hat{\mathbf{u}}_f}{\partial \hat{t}} + (\hat{\mathbf{u}}_f \cdot \hat{\nabla})\hat{\mathbf{u}}_f \right) \quad = \quad -\hat{\nabla}\hat{p}_f + \hat{\nabla} \cdot \hat{\tau}_f + \hat{\rho}_f (1 - \phi)\hat{g}\boldsymbol{k} - \hat{\mathbf{m}}. \tag{2.11}$$

Where $\hat{\mathbf{\Sigma}}_p$ denotes the particle stress tensor, which may be further decomposed into shear and normal stress components. The fluid phase shear stress tensor is denoted $\hat{\tau}_f$ and $\hat{\mathbf{m}}$ denotes the solid-liquid interaction force, per unit mass.

Normally however, we are concerned with the bulk mixture momentum equation, written as the sum of the (2.10) and (2.11). We also assume that the flow varies slowly in the axial direction, due to variations in mean solids concentration. For a fully developed turbulent flow, the averaged components of the inertial components on the left hand side of (2.10) and (2.11) vanish, leaving only Reynolds stress terms on the the right-hand side. The solid-liquid interaction terms cancel out. We write this simplified mixture momentum balance as:

$$0 = -\hat{\nabla}\hat{p} + \hat{\nabla} \cdot \hat{\tau} + \hat{\rho}\hat{g}\boldsymbol{k}, \tag{2.12}$$

where we decompose the shear stress tensor $\hat{\tau}$ into a viscous term and a turbulent term, i.e.

$$\hat{\tau} = \hat{\tau}^v + \hat{\tau}^t. \tag{2.13}$$

2.1.3 Viscous stress closure

The approach adopted for modelling the viscous stress tensor is outlined in [18]. The fracking fluid is assumed to be of Herschel-Bulkley type. We follow the developments of Ovarlez and co-workers, [3, 5, 26, 31, 32, 47], who have used a mix of experimental and modelling techniques in developing a general framework that has been validated in some limits for non-Newtonian suspension flows. The general framework is as follows.

Shear flows of suspensions are characterised by a bulk suspension viscosity $\hat{\eta}$, which relates to the viscosity of the mixture of solid and liquid phases and is used to model the viscous component of the shear stress tensor in a conventional way, i.e.

$$\hat{\tau}^v = \hat{\eta}\hat{\dot{\gamma}}(\hat{\bar{\mathbf{u}}}), \tag{2.14}$$

where $\hat{\dot{\gamma}}(\hat{\bar{\mathbf{u}}})$ is the rate of strain tensor. The suspension viscosity is first de-

composed as follows

$$\hat{\eta} = \hat{\eta}_f \eta_r(\bar{\phi}), \tag{2.15}$$

where $\hat{\eta}_f$ is referred to as the liquid phase viscosity and $\eta_r(\bar{\phi})$ is the dimensionless relative viscosity. We will assume dependency on the ensemble averaged solid fraction $\bar{\phi}$ rather than on ϕ, as we wish to work with the averaged quantities. This decomposition of the suspension viscosity is quite classical and the relative viscosity is modeled by a closure law, e.g. most simply the Einstein-Roscoe law. Since here we deal with significant $\bar{\phi}$, we suggest adopting the Krieger-Dougherty law:

$$\eta_r(\bar{\phi}) = \left[1 - \frac{\bar{\phi}}{\phi_m}\right]^{-2.5\phi_m}, \tag{2.16}$$

or one of its close variants, e.g. [12, 21, 27, 34]. Apart form conceptual simplicity, there exist generalisations to particles of different shapes e.g. rods/fibres, see [49]. For the results presented in this thesis we will assume a maximal packing fraction of $\phi_m = 0.57$.

The relative viscosity can be further decomposed to model the solid phase stress tensor, but this is not needed here. For the liquid phase viscosity $\hat{\eta}_f$, two effects must be considered. Firstly, the fluids are shear-thinning and secondly the particles modify the viscosity. In the absence of particles the effective viscosity is given by a constitutive law that depends on the rate of strain, i.e. the pure fracking fluid has effective viscosity:

$$\hat{\eta}_{f,0}(\hat{\dot{\gamma}}_{loc}) = \hat{\kappa}_0 \hat{\dot{\gamma}}_{loc}^{n-1} + \frac{\hat{\tau}_{Y0}}{\hat{\dot{\gamma}}_{loc}}, \tag{2.17}$$

where $\hat{\kappa}_0$, $\hat{\tau}_{Y0}$ and n are the consistency, the yield stress and the power law index of the pure fracking fluid, respectively. Here $\hat{\dot{\gamma}}_{loc}$ denotes the (local) strain rate of the fluid.

A significant contribution of Ovarlez and co-workers is in recognising that although the solids phase increases the viscosity of the suspension via $\eta_r(\bar{\phi})$, the

presence of particles also reduces the viscosity of the inter-particle fluid, when it is shear-thinning. We denote the bulk suspension strain rate by $\hat{\dot{\gamma}}$, which is computed as the second invariant of the tensor $\hat{\dot{\gamma}}(\hat{\bar{\mathbf{u}}})$. The main point is that $\hat{\dot{\gamma}}$ is effectively amplified by the presence of particles, since velocity gradients are concentrated only within the liquid phase. Ovarlez and co-workers have developed the following law to describe this amplification:

$$\hat{\dot{\gamma}}_{loc} = \left[\frac{\eta_r(\bar{\phi})}{1-\bar{\phi}}\right]^{1/2} \hat{\dot{\gamma}}, \tag{2.18}$$

which is verified reasonably well by experimental results [26, 31] and also agrees with theoretical considerations, [3].

This leads to the following definition of the liquid phase viscosity $\hat{\eta}_f$:

$$\hat{\eta}_f(\hat{\dot{\gamma}}, \bar{\phi}) = \hat{\eta}_{f,0}(\hat{\dot{\gamma}}_{loc}(\bar{\phi})) = \hat{\kappa}_0 \left[\frac{\eta_r(\bar{\phi})}{1-\bar{\phi}}\right]^{(n-1)/2} \hat{\dot{\gamma}}^{n-1} + \frac{\hat{\tau}_{Y0}}{\hat{\dot{\gamma}}} \left[\frac{\eta_r(\bar{\phi})}{1-\bar{\phi}}\right]^{-1/2}. \tag{2.19}$$

This can also be interpreted as assuming that the liquid within the suspension obeys a Herschel-Bulkley type law, but with $\bar{\phi}$-dependent consistency and yield stress defined by:

$$\hat{\kappa} = \hat{\kappa}_0 \left[\frac{\eta_r(\bar{\phi})}{1-\bar{\phi}}\right]^{(n-1)/2} \qquad \hat{\tau}_Y = \frac{\hat{\tau}_{Y0}}{\left[\frac{\eta_r(\bar{\phi})}{1-\bar{\phi}}\right]^{1/2}}. \tag{2.20}$$

The framework given by (2.15)-(2.21) is quite simple to work with and modify.

Alternatively, we can include directly the bulk viscousification effect of the relative viscosity to get:

$$\hat{\kappa}_s(\bar{\phi}) = \hat{\kappa}_0 Y(\bar{\phi}) \qquad \hat{\tau}_{Ys}(\bar{\phi}) = \hat{\tau}_{Y0} X(\bar{\phi}) \tag{2.21}$$

$$X(\bar{\phi}) = \sqrt{(1-\bar{\phi})\eta_r(\bar{\phi})} \qquad Y(\bar{\phi}) = \eta_r(\bar{\phi}) \left[\frac{\eta_r(\bar{\phi})}{1-\bar{\phi}}\right]^{(n-1)/2}$$

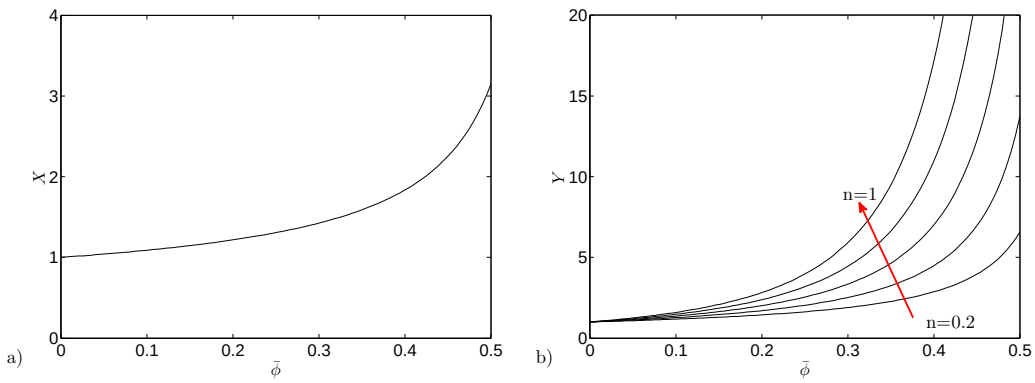

Figure 2.1: a) X vs $\bar{\phi}$; b) Y vs $\bar{\phi}$ for $n = 0.2, 0.4, 0.6, 0.8, 1.0$.

Therefore, we can write the effective suspension viscosity as follows

$$\hat{\eta}(\hat{\dot{\gamma}}, \bar{\phi}) = \hat{\kappa}_s \left[\frac{\eta_r(\bar{\phi})}{1-\bar{\phi}}\right]^{(n-1)/2} \hat{\dot{\gamma}}^{n-1} + \frac{\hat{\tau}_{Ys}}{\hat{\dot{\gamma}}} \left[\frac{\eta_r(\bar{\phi})}{1-\bar{\phi}}\right]^{-1/2}. \tag{2.22}$$

Figure 2.1 plots the functions $X(\bar{\phi})$ and $Y(\bar{\phi})$ that describe the amplification of the yield stress and consistency within the suspension. In all cases we see a viscousification effect as $\bar{\phi}$ increases. Note however, that this is as a result of the relative viscosity: on neglecting the final multiplication by $\eta_r(\bar{\phi})$, the functions in (2.21) are decreasing with $\bar{\phi}$,i.e., local viscosity on particle scale (2.17) is decreasing with $\bar{\phi}$, due to shear rate amplification by particles.

2.1.4 Turbulent velocity closure

We consider fully turbulent flow along a vertical pipe. The ensemble-averaged solids fraction $\bar{\phi}$ is assumed uniform across the pipe. The following system of

equations governs the flow of the mixture:

$$0 = -\frac{\partial \hat{p}}{\partial \hat{z}} + \frac{1}{\hat{r}}\frac{\partial}{\partial \hat{r}}(\hat{r}\hat{\tau}_{rz}) + \hat{\rho}\hat{g}, \tag{2.23}$$

$$0 = -\frac{\partial \hat{p}}{\partial \hat{r}} + \frac{1}{\hat{r}}\frac{\partial}{\partial \hat{r}}(\hat{r}\hat{\tau}_{rr}), \tag{2.24}$$

$$0 = \frac{1}{\hat{r}}\frac{\partial}{\partial \hat{r}}(\hat{r}\hat{\bar{u}}) + \frac{\partial \hat{\bar{w}}}{\partial \hat{z}}, \tag{2.25}$$

where $\hat{\tau}_{rz}$ and $\hat{\tau}_{rr}$ can be decomposed to viscous and turbulent parts. The viscous component has been discussed above. The turbulent component arises from Reynolds stress terms, approximated as follows:

$$\hat{\tau}_{rz} = \hat{\tau}^v_{rz} + \hat{\tau}^t_{rz} = \hat{\tau}^v_{rz} - \hat{\rho}\overline{(\hat{u}'\hat{w}')}, \tag{2.26}$$

$$\hat{\tau}_{rr} = \hat{\tau}^v_{rr} + \hat{\tau}^t_{rr} = \hat{\tau}^v_{rr} - \hat{\rho}\overline{(\hat{u}'\hat{u}')}. \tag{2.27}$$

We assume that the Reynolds stress ($\hat{\tau}^t_{rr}$) is independent of z and the modified pressure gradient

$$\frac{\partial \hat{P}}{\partial \hat{z}} = \frac{\partial \hat{p}}{\partial \hat{z}} - \hat{\rho}\hat{g},$$

is constant across the pipe cross-section. We integrate equation (2.23) from wall of the pipe $\hat{y} = 0$ outwards:

$$\hat{\tau}^t_{rz} + \hat{\tau}^v_{rz} = \hat{\tau}_w + \frac{\hat{y}}{2}\frac{\partial \hat{P}}{\partial \hat{z}} : \qquad \hat{\tau}_w = -\frac{\hat{R}}{2}\frac{\partial \hat{P}}{\partial \hat{z}}. \tag{2.28}$$

Note that $\hat{\tau}_w$ is the wall shear stress and $\hat{y}$ is $\hat{R} - \hat{r}$. This is used to define a turbulent velocity scale $\hat{W}^*$:

$$\hat{\tau}^v_w = \hat{\rho}(\hat{W}^*)^2. \tag{2.29}$$

We substitute (2.29) into (2.28) to give

$$\hat{\tau}^t_{rz} + \hat{\tau}^v_{rz} \quad = \quad \hat{\rho}(\hat{W}^*)^2 \left(1 - \frac{\hat{y}}{\hat{R}}\right). \tag{2.30}$$

The viscous stress is mainly large in the vicinity of the wall, where $\hat{\tau}^t_{rz}$ is small. According to [38], the proper scaling factor for $\hat{\tau}^v_{rz}$ is:

$$\hat{\tau}^v_{rz} = \hat{\mu}_w \frac{\partial \hat{\bar{w}}}{\partial \hat{y}} : \qquad \hat{\mu}_w = \frac{\hat{\tau}_w}{[(\hat{\tau}_w - \hat{\tau}_{Ys})/\hat{\kappa}_s]^{1/n}}. \tag{2.31}$$

In the core region of the pipe where Reynolds stress is dominant, we define $y = \hat{y}/\hat{R}$ and scale the Reynolds stress: $\tau^t_{rz} = \hat{\tau}^t_{rz}/[\hat{\rho}(\hat{W}^*)^2]$, to give:

$$\tau^t_{rz} + \frac{1}{Re^*}\frac{\partial}{\partial y}\left(\frac{\hat{\bar{w}}}{\hat{W}^*}\right) \quad = \quad (1 - y). \tag{2.32}$$

The Reynolds number Re^* is defined by:

$$Re^* = \frac{\hat{\rho}\hat{W}^*\hat{R}}{\hat{\mu}_w}.$$

We typically expect that $Re^* \gg 1$ when fully turbulent, meaning that the viscous stresses are largely irrelevant in the core.

On the other hand, the stress at the pipe wall is purely viscous, so that the scaling for (2.32) can not be valid near the wall in the limit $Re^* \to \infty$. From (2.32) we conclude that the near-wall behaviour can be accounted for by absorbing Re^* in the scaling for $\hat{y}$, i.e. $y^+ = yRe^* = \hat{y}\hat{W}^*\hat{\rho}/\hat{\mu}_w$. The resulting equation is

$$\tau^t_{rz} + \frac{\partial}{\partial y^+}\left(\frac{\hat{\bar{w}}}{\hat{W}^*}\right) \quad = \quad (1 - \frac{y^+}{Re^*}). \tag{2.33}$$

When the production and dissipation of the mixture turbulent energy are

equal (i.e. in a state of local equilibrium, see [43]), we may write

$$-<\hat{u}'\hat{w}'>(\frac{\partial\hat{\bar{w}}}{\partial\hat{y}})\approx\frac{W^{*3}}{\hat{R}}\quad\texttt{as}\quad Re^*\to\infty:-\frac{<\hat{u}'\hat{w}'>}{W^{*2}}=(1-y)$$
$$\Rightarrow\frac{\partial\hat{\bar{w}}}{\partial\hat{y}}=\frac{W^*}{\hat{R}}\frac{\partial F(y)}{\partial y}. \quad (2.34)$$

Equation (2.33) implies that $\hat{w}/W^* = G(y^+)$ and consequently $\partial\hat{\bar{w}}/\partial\hat{y} = (W^*Re^*/\hat{R})(\partial G/\partial y^+)$. In the limit that $y^+ \to \infty$ and $y \to 0$, we may write

$$\frac{W^*}{R}\frac{\partial F(y)}{\partial y}=\frac{W^*Re^*}{R}\frac{\partial G}{\partial y^+}\Rightarrow\frac{y^+}{n}\frac{\partial G}{\partial y^+}=\frac{y}{n}\frac{\partial F}{\partial y}=\frac{1}{\kappa n}. \quad (2.35)$$

Finally, we have

$$\frac{\hat{\bar{w}}}{\hat{W}^*}=\frac{1}{\kappa_1 n}\ln y^{+n}+\frac{\kappa_2}{n}. \quad (2.36)$$

Note that the log-law is valid in the matching region where $y^+ \to \infty$ and $y \to 0$. However, this is an engineering approximation to consider the log-law velocity profile for the whole cross section of the pipe. Following [38], who study weakly turbulent power law and Herschel-Bulkley fluids using DNS techniques, the suggested values for the constants in (2.36) are $\kappa_1 = 0.4$ and $\kappa_2 = 5.5$.

We assume that the dimensionless flow rate across the pipe is π in order to calculate W^*. We define the friction factor in the usual way:

$$f_f = 2(\hat{W}^*/\hat{U}_0)^2,$$

where $\hat{U}_0$ is the mean velocity of the mixture. Then we scale $\bar{w} = \hat{\bar{w}}/\hat{U}_0$ and

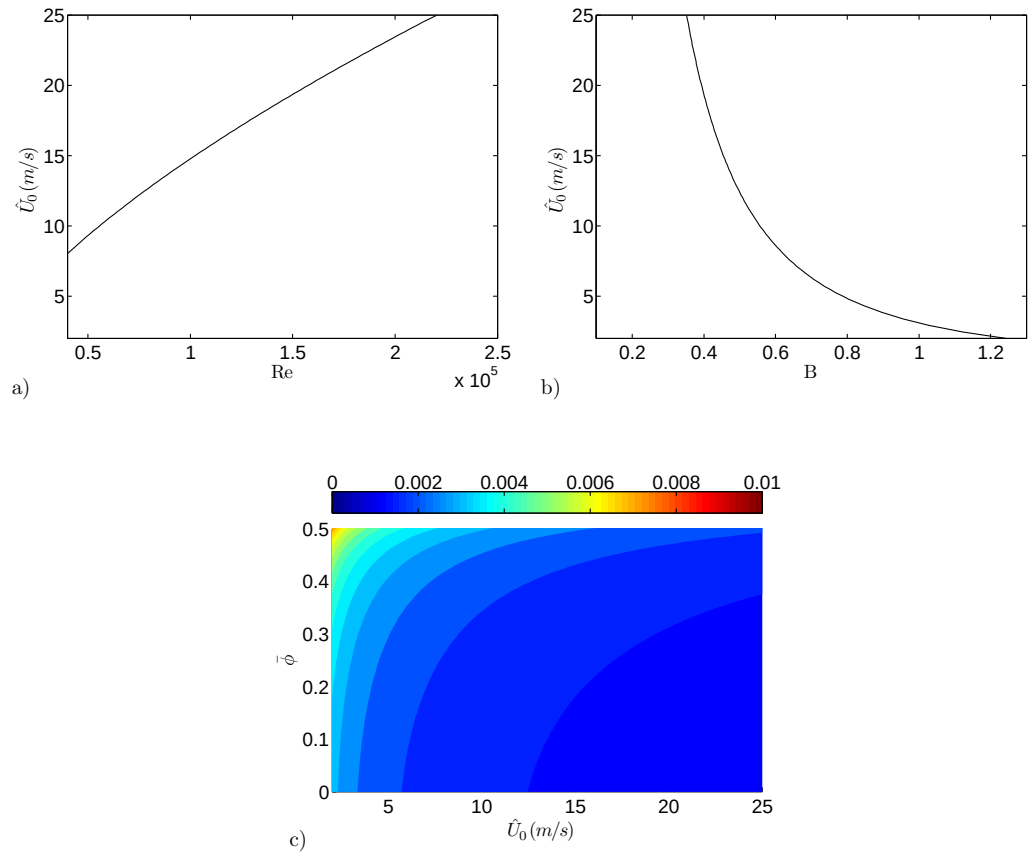

Figure 2.2: a) & b) Dependency of bulk Re and B on mean flow; c) colormap of friction factor in $(\hat{U}_0, \bar{\phi})$ plane (see equation 2.38). For all figures, we have $n = 0.5$, $\hat{K}_0 = 0.1\text{Pa.s}^n$, $\hat{\tau}_{Y0} = 1\text{Pa}$, $s = 2.65$, $\hat{D} = 62\text{mm}$.

write (2.36) in the following dimensionless form.

$$\bar{w} = \sqrt{0.5 f_f}\left(\frac{\kappa_2}{n} + \frac{1}{\kappa_1}\ln\left[(1-r)Re_w(0.5 f_f)^{1/2}\right]\right), \tag{2.37}$$

where $r = \hat{r}/\hat{R}$ and

$$Re_w = \frac{\hat{\rho}\hat{R}\hat{U}_0}{\hat{\mu}_w}.$$

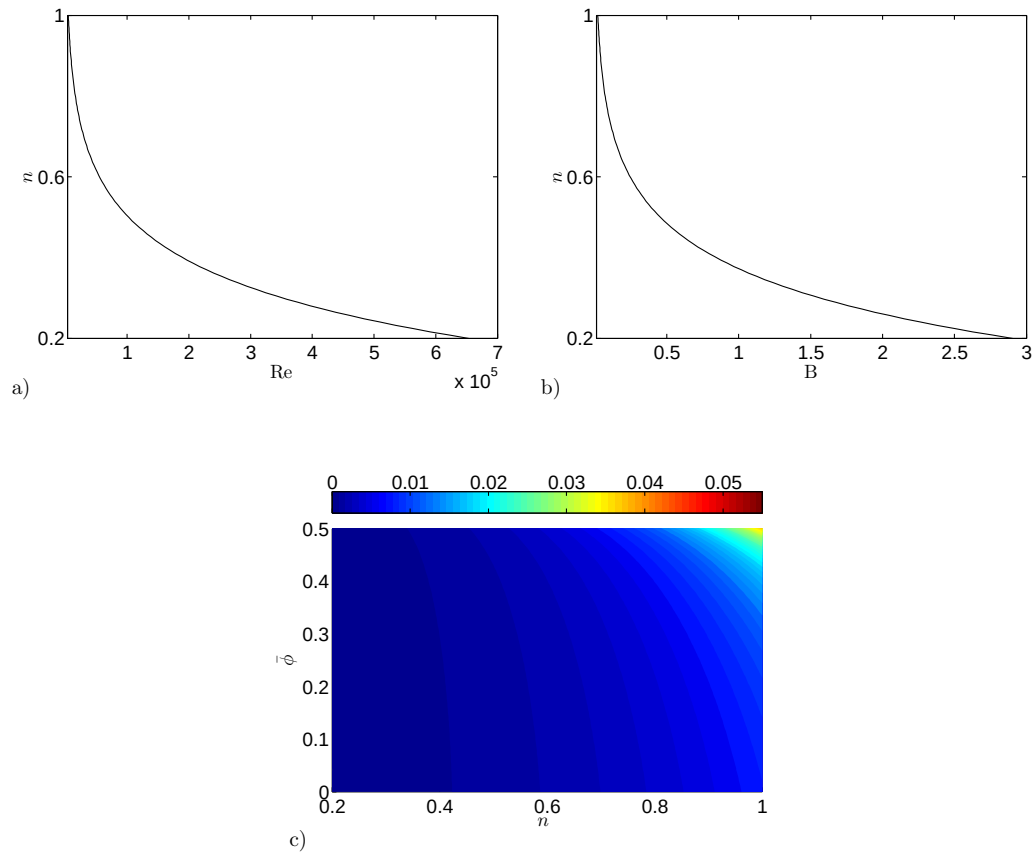

Figure 2.3: a) & b) Dependency of bulk Re and B on power law index n; c) colormap of friction factor in $(n, \bar{\phi})$ plane (see equation 2.38). For all figures, we have $\hat{U}_0 = 15$m/s, $\hat{K}_0 = 0.1$Pa.s^n, $\hat{\tau}_{Y0} = 1$Pa, $s = 2.65$, $\hat{D} = 62$mm.

In order for the flow to be fully turbulent, it is expected that $Re_w \gg 1$. To compute the friction factor, we integrate across the pipe cross-section, using the constraint that the flow rate is π, or the mean velocity is unity:

$$1 = \int_0^1 2r\bar{w}(r)\ \mathrm{d}r.$$

This gives us, at leading order:

$$1 = \sqrt{0.5 f_f}\left(\frac{\kappa_2}{n} + \frac{1}{\kappa_1}\ln\left[Re_w(0.5 f_f)^{1/2}\right] - \frac{1.5}{\kappa_1}\right), \tag{2.38}$$

We obtain the dependency of Re_w on the dimensionless parameters of the bulk flow as follows.

$$Re_w = \frac{Re^{1/n}}{0.5 f_f}\left[\left(\frac{0.5 f_f}{Y(\bar{\phi})}\right)(s\phi + 1 - \phi) - \left(\frac{B}{Re}\frac{X(\bar{\phi})}{Y(\bar{\phi})}\right)\right]^{1/n}. \tag{2.39}$$

Equation (2.39) is obtained by expressing mean flow velocity and stress in (2.38) in terms of bulk Re and B. Where, B is $\hat{\tau}_{Y0}/\hat{\kappa}_0(\hat{U}_0/\hat{R})^n$ and Re is $\hat{\rho}_f\hat{U}_0^2/\hat{\kappa}_0(\hat{U}_0/\hat{R})^n$. Two additional important effects that one might try to add are: (i) some form of depletion of the particle phase near the wall; (ii) wall roughness effects. Both these effects are however most likely to be significant with respect to dispersion only for weakly turbulent flows, when the wall layers become thicker.

Figures 2.2a & b show the the dependency of bulk Re and B on the velocity of mean flow $\hat{U}_0$ respectively. Re increases with the velocity of mean flow because both inertia and shear rate increase in the system. The fluid is shear thinning the latter decreases the viscosity. The total stress increases with the velocity of mean flow and consequently B decreases. Figure 2.2c shows the colormap of f_f in the $(\phi, \hat{U}_0)$ plane. We see that the friction factor increases with the solids volume fraction as a result of viscousification. Moreover, the friction factor decreases with velocity of mean flow. Although total stress increases with $\hat{U}_0$, the ratio of $\hat{W}^*/\hat{U}_0$ decreases with $\hat{U}_0$.

Figure 2.3 shows similar results, but with variations in n rather than $\hat{U}_0$. Figures 2.3a & b show that the bulk Re and B decrease with n. The reason is that the viscous stress increases with n. Figure 2.3c shows that the friction factor increases with both the solids volume fraction and n as a result of viscousification.

2.1.5 Relative velocity closure

In this section, we develop the closure for $\hat{\mathbf{m}}$ in terms of the relative velocity between solid and fluid phases, $\hat{\bar{\mathbf{u}}}_r$, and $\bar{\phi}$. Principally this involves hydrodynamic effects of viscous drag:

$$\hat{\mathbf{m}} \approx \hat{\mathbf{F}}_D \frac{6\bar{\phi}}{\pi \hat{d}_p^3}. \tag{2.40}$$

where

$$\hat{\mathbf{F}}_D = -\frac{\hat{\rho}_f}{2}|\hat{\bar{\mathbf{u}}}_r|\hat{\bar{\mathbf{u}}}_r(\pi \hat{d}_p^2/4)C_D. \tag{2.41}$$

The interaction term is also estimated from combining (2.10) and (2.11):

$$\hat{\mathbf{m}} = -\phi(1-\phi)[\hat{\rho}_s - \hat{\rho}_f]\hat{g}\boldsymbol{k} + \phi(1-\phi)\left[\hat{\rho}_s \frac{D_p \hat{\mathbf{u}}_p}{D\hat{t}} - \hat{\rho}_f \frac{D_f \hat{\mathbf{u}}_f}{D\hat{t}}\right] - (1-\phi)\hat{\nabla}\cdot\hat{\boldsymbol{\Sigma}}_p + \phi[-\hat{\nabla}\hat{p}_f + \hat{\nabla}\cdot\hat{\tau}_f]. \tag{2.42}$$

It is usual to assume that the first term is dominant, leading to:

$$|\hat{\bar{\mathbf{u}}}_r|\hat{\bar{\mathbf{u}}}_r = \frac{4}{3C_D}(1-\phi)(s-1)\hat{g}\hat{d}_p \tag{2.43}$$

Despite numerous studies on the motion of a particle in Newtonian fluids, there are only a limited number of studies on the motion of an object in the yield stress fluids. As well as non-Newtonian effects, we need to incorporate the effect of the particles on the settling, i.e. via hindering. The approach that we adopt follows that of [32]. We compute the single particle settling speed from (2.43). Similar to a Newtonian fluid we adopt a drag coefficient closure such as:

$$C_D = \frac{24}{Re_p}(1 + 0.1 Re_p^{0.75}); \tag{2.44}$$

see e.g. [20]. Here $Re_p = \hat{\rho}_f|\hat{\bar{\mathbf{u}}}_r|\hat{d}_p/\hat{\eta}_f$. Recall that $\hat{\eta}_f$ is the liquid phase viscosity around the particles; see (2.19). Combining (2.44) with (2.43) leads to a unique determination of the relative velocity for a single particle, say $\hat{\bar{\mathbf{u}}}_{r,0}$.

For example, assuming $N_{Re} \ll 1$ we have the Stokes solution:

$$\hat{\bar{\mathbf{u}}}_{r,0} = \frac{1}{18}(1-\phi)(s-1)\frac{\hat{\rho}_f \hat{g} \hat{d}_p^2}{\hat{\eta}_f}. \tag{2.45}$$

The single particle settling velocity is now multiplied by a hindering function $h(\bar{\phi})$, to give the relative velocity of the suspension, i.e.

$$\hat{\bar{\mathbf{u}}}_r = h(\bar{\phi})\hat{\bar{\mathbf{u}}}_{r,0}. \tag{2.46}$$

Following [32], we use

$$h(\phi) = \frac{1-\phi}{\eta_r(\phi)}. \tag{2.47}$$

A similar approach has been adopted by [41].

It remains to specify the suspension shear rate within the turbulent flow, which is needed to evaluate the effective viscosity $\hat{\eta}_f$. Close to the walls, the velocity changes from $\hat{U}_0$ to zero over approximately the length-scale of the viscous sublayer, i.e. an effective shear rate would be something like:

$$\hat{\dot{\gamma}} \;=\; \frac{|\hat{\bar{\mathbf{u}}}_r|}{\hat{d}_p} + \frac{\hat{U}_0}{\hat{y}_{sub}} \tag{2.48}$$

However, at high Reynolds numbers the viscous the wall region has only a minor effect on dispersion, compared with the turbulent core. In the core, there are both changes in mean flow (with shear rate roughly $\sim \hat{W}^*\hat{D}$), and in the fluctuating component of the velocity. A very simple model is to assume the velocity fluctuations of size $\sim \hat{W}^*$ occur on a scale of the largest eddies, assumed to have size roughly $0.1\hat{D}$. This leads to:

$$\hat{\dot{\gamma}} \;\approx\; \frac{|\hat{\bar{\mathbf{u}}}_r|}{\hat{d}_p} + \frac{\hat{W}^*}{0.1\hat{D}}. \tag{2.49}$$

Note that this model suggests that the strain rates due to the velocity fluctu-

ations are probably the dominant component in the turbulent core (compared to gradients in the mean velocity), which has the consequence that the relative velocity will vary with $\hat{r}$ only due to variations in $\bar{\phi}$.

Figure 2.4 shows colourmaps of various flow parameters in the $(\hat{U}_0, \bar{\phi})$ plane. We note that the total shear rate increases with both $\hat{U}_0$ and $\bar{\phi}$. The former is due to increase in bulk shear rate and the latter is as a result of shear rate amplification by particles. We calculated $\hat{\dot{\gamma}}$ for a range of flow parameters and observed that the main contribution to $\hat{\dot{\gamma}}$ comes from background shear rate, i.e. the second term in (2.49). Since the suspension is shear thinning, $\hat{\eta}(\hat{\dot{\gamma}})$ is a decreasing function of $\hat{\dot{\gamma}}$. On the particle scale, we see that the relative velocity, $\hat{\bar{\mathbf{u}}}_r$, decreases with viscousification (i.e. the increase in $\bar{\phi}$) and increases with liquefaction (i.e. the increase in $\hat{U}_0$ and bulk shear rate). Therefore, we see that Re_p decreases with $\bar{\phi}$ and increases with $\hat{U}_0$.

Figure 2.5 shows colourmaps of various flow parameters in the $(\hat{d}_p, \bar{\phi})$ plane. Note that the friction factor (2.38) and hence $\hat{W}^*$ do not depend on the size of particles, $\hat{d}_p$. Since, $\hat{\dot{\gamma}}$ mainly originates from the background shear rate, i.e. $\hat{W}^*/0.1\hat{D}$, we can conclude that the total shear rate, $\hat{\dot{\gamma}}$, and suspension viscosity, $\hat{\eta}(\hat{\dot{\gamma}})$, will have only a small variation with $\hat{d}_p$. The settling velocity of particles does however increase with the particle size due to the volumetric increase in gravity force. Therefore, $\hat{\bar{\mathbf{u}}}_r$ and consequently Re_p are increasing functions of the particle size.

2.2 Particle dispersion

In most pipeline transport processes, spreading of a concentration (e.g. solids fraction), is governed by a number of contributions, from both diffusive and advective processes. In the case of fully turbulent flows in moderately long pipes, it is possible to estimate the net effect of the advective component in spreading concentrations axially, in what has been termed Taylor dispersion [42]. The net effect of axial spreading by advection results in diffusion of the

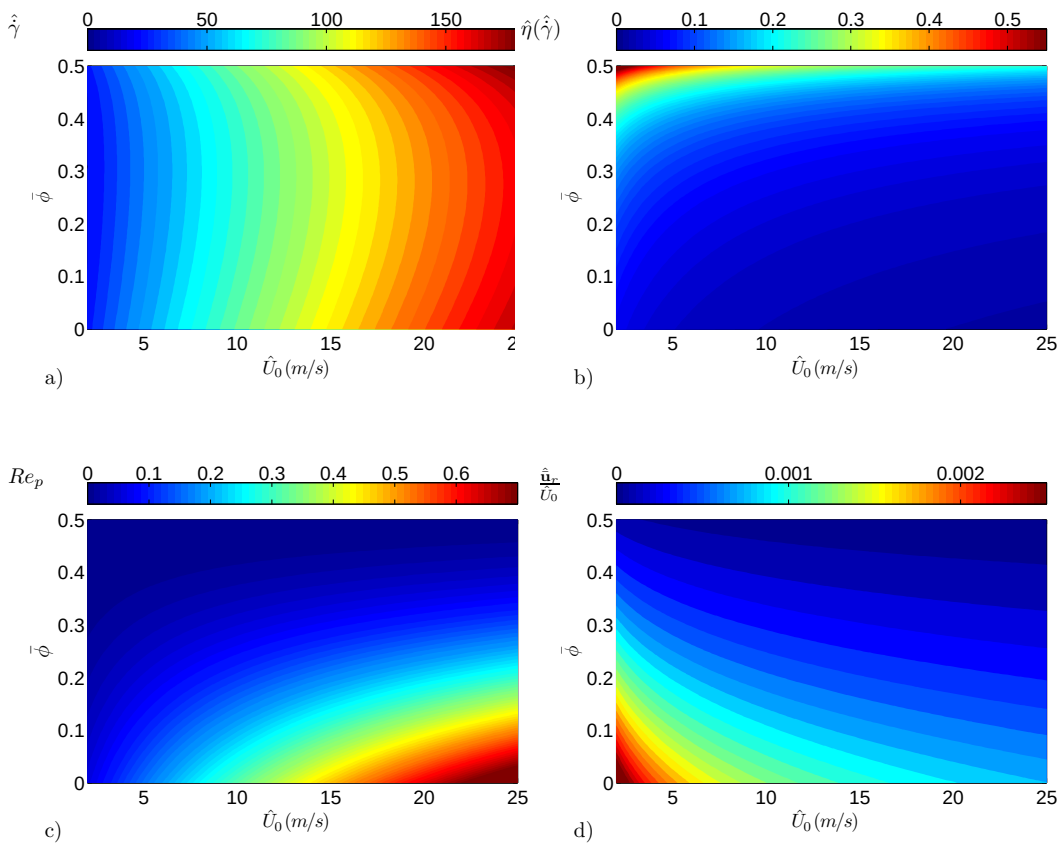

Figure 2.4: Colourmaps of various flow parameters plotted in the $(\hat{U}_0, \bar{\phi})$ plane: a) total shear rate, $\hat{\dot{\gamma}}(1/s)$, as calculated from equation (2.49); b) effective viscosity of the suspension, $\hat{\eta}(\hat{\dot{\gamma}})(Pa.s)$, as calculated from (2.22); c) particle Re number, Re_p; d) dimensionless slip velocity $\hat{\mathbf{u}}_r/\hat{U}_0$, as calculated from (2.43). For all figures, we have $n = 0.5$, $\hat{K}_0 = 0.1$Pa.s^n, $\hat{\tau}_{Y0} = 1$Pa, $s = 2.65$, $\delta_p = 0.01$, $\hat{D} = 62$mm.

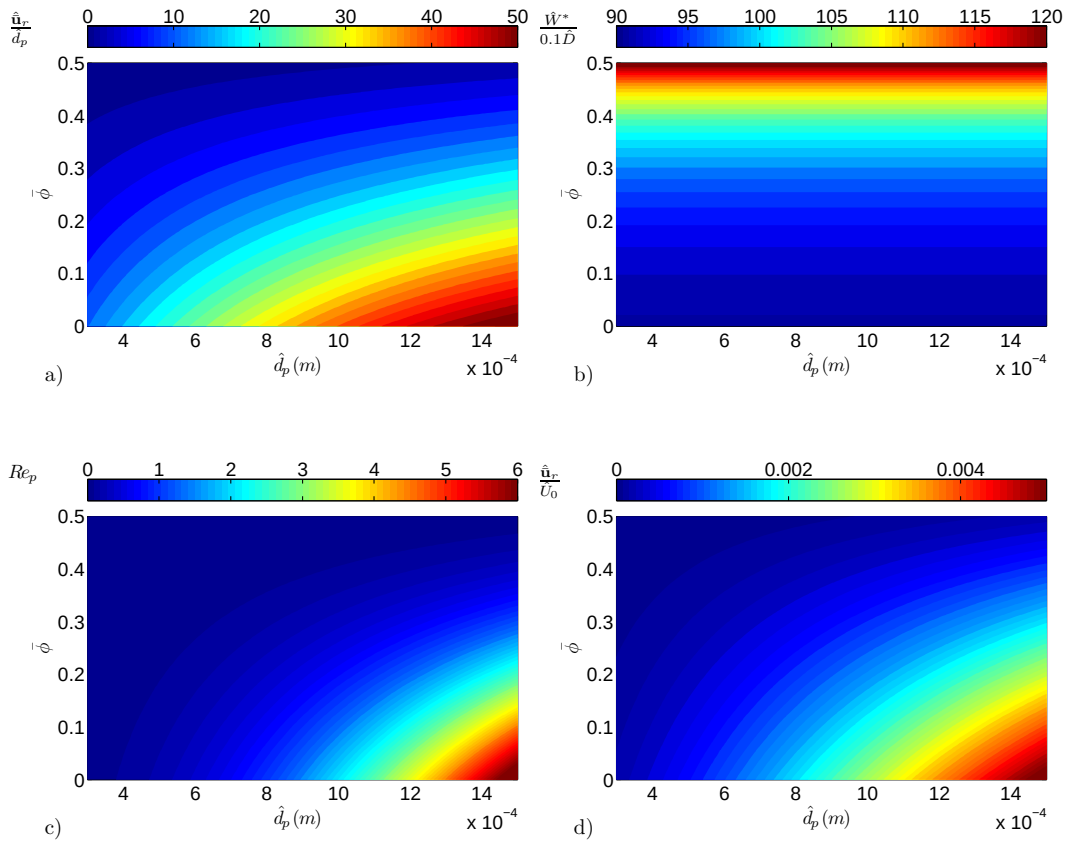

Figure 2.5: Colourmaps of various flow parameters plotted in the $(d_p, \bar{\phi})$ plane: a) particle shear rate $\frac{\hat{\dot{\mathbf{u}}}_r}{\hat{d}_p}$; b) background shear rate $\frac{\hat{W}^*}{0.1\hat{D}}$; c) particle Reynolds number, Re_p; d) dimensionless slip velocity $\hat{\dot{\mathbf{u}}}_r/\hat{U}_0$, as calculated from (2.43). For all figures, we have $\hat{U}_0 = 15$m/s, $n = 0.5$, $\hat{K}_0 = 0.1$Pa.s^n, $\hat{\tau}_{Y0} = 1$Pa, $s = 2.65$, $\hat{D} = 62$mm.

mean concentration, relative to a constant advective speed. Importantly, the Taylor dispersion effect dominates diffusivity effects. In this section, below we develop the general expression for the Taylor dispersion effect, applied to the solids fraction $\bar{\phi}$. Later we compute the net diffusive effects for 3 different particle diffusivity models, and give estimates for the length of pipe over which a slug of proppant would disperse in travelling down the pipe.

2.2.1 Dispersion model

Following the analysis of §2.1.4, the mean axial velocity in the turbulent core is given by:

$$\hat{\bar{w}} = \hat{W}^* \left(\frac{1}{\kappa_1 n} \ln y^{+n} + \frac{\kappa_2}{n} \right), \tag{2.50}$$

which is coupled to the mean solids fraction $\bar{\phi}$ through the rheological closures entering the wall-coordinate scaling for y^+. The mean velocity and solids fraction satisfy:

$$0 = \frac{1}{\hat{r}} \frac{\partial}{\partial \hat{r}} (\hat{r} \hat{\bar{u}}) + \frac{\partial \hat{\bar{w}}}{\partial \hat{z}}, \tag{2.51}$$

$$\frac{\partial \bar{\phi}}{\partial \hat{t}} + \hat{\bar{u}} \frac{\partial \bar{\phi}}{\partial \hat{r}} + \hat{\bar{w}} \frac{\partial \bar{\phi}}{\partial \hat{z}} + \frac{\partial \hat{\Lambda}}{\partial \bar{\phi}} \frac{\partial \bar{\phi}}{\partial \hat{z}} = \frac{1}{\hat{r}} \frac{\partial}{\partial \hat{r}} (\hat{r} \hat{D}_d \frac{\partial \bar{\phi}}{\partial \hat{r}}) + \frac{\partial}{\partial \hat{z}} (\hat{D}_d \frac{\partial \bar{\phi}}{\partial \hat{z}}), \tag{2.52}$$

where $\hat{\Lambda} = \bar{\phi}(1 - \bar{\phi}) \hat{\bar{w}}_r$.

We assume that $\hat{D}_d = \hat{D}_d(\hat{r}, \bar{\phi})$ and write:

$$\hat{D}_d(\hat{r}, \bar{\phi}) = \hat{D}_{d,ave} D_d(\hat{r}, \bar{\phi}) : \qquad \hat{D}_{d,ave} = \frac{2}{\phi_{\max}} \int_0^{\phi_{\max}} \int_0^{\hat{R}} \hat{D}_d(\hat{r}, \bar{\phi}) \hat{r} \, \mathrm{d}\hat{r} \mathrm{d}\bar{\phi},$$

with $\phi_{\max}$ some upper limit for $\bar{\phi}$. We use the averaged particle diffusivity to

define a Péclet number Pe via:

$$Pe = \frac{\hat{R}\hat{U}_0}{\hat{D}_{d,ave}}. \tag{2.53}$$

Note that typically the Péclet number is larger than unity (approximately scaling with a negative fractional power of the friction factor, depending on the model used - see below). The Péclet number can be interpreted as the number of radii that the mixture needs to advect at mean speed in order for the particle diffusivity to diffuse the solids concentration across the pipe. Although greater than unity, it is also common that $\delta Pe \ll 1$, since pipe aspect ratios are relatively long.

Equations (2.51) , (2.52) and the velocity profile are made dimensionless with the following scaling:

$$z = \frac{\hat{z}}{\hat{L}}, \quad r = \frac{\hat{r}}{\hat{R}}, \quad t = \hat{t}\frac{\hat{U}_0}{\hat{L}}, \quad \bar{u} = \frac{2\hat{\bar{u}}}{\delta\hat{U}_0}, \quad \bar{w} = \frac{\hat{\bar{w}}}{\hat{U}_0}, \quad \bar{w}_r = \frac{\hat{\bar{w}}_r}{\hat{U}_0}, \quad \Lambda = \frac{\hat{\Lambda}}{\hat{U}_0}, \quad \sqrt{0.5 f_f} = \frac{\hat{W}^*}{\hat{U}_0}.$$

On substituting the non-dimensional variables into the governing equations, we arrive at:

$$\bar{w} = \sqrt{0.5 f_f}\left(\frac{\kappa_2}{n} + \frac{1}{\kappa_1}\ln\left[(1-r)Re_w(0.5 f_f)^{1/2}\right]\right), \tag{2.54}$$

$$0 = \frac{1}{r}\frac{\partial}{\partial r}(r\bar{u}) + \frac{\partial \bar{w}}{\partial z}, \tag{2.55}$$

$$\frac{\delta Pe}{2}\left[\frac{\partial\bar{\phi}}{\partial t} + \bar{u}\frac{\partial\bar{\phi}}{\partial r} + \bar{w}\frac{\partial\bar{\phi}}{\partial z} + \frac{\partial\Lambda}{\partial\bar{\phi}}\frac{\partial\bar{\phi}}{\partial z}\right] = \frac{1}{r}\frac{\partial}{\partial r}(rD_d\frac{\partial\bar{\phi}}{\partial r}) + \frac{\delta^2}{4}\frac{\partial}{\partial z}\left(D_d\frac{\partial\bar{\phi}}{\partial z}\right) \tag{2.56}$$

Recall that $\delta = \hat{D}/\hat{L} = 2\hat{R}/\hat{L}$.

Note that by construction, $D_d(r,\bar{\phi}) \sim 1$ and the average of the mean axial velocity $\bar{w}$ across the pipe is 1. We now define the averaged and fluctuating

settling rates:

$$\bar{w}_{r,ave} = \int_0^1 2r \frac{\partial \Lambda(\bar{\phi})}{\partial \bar{\phi}} \, \mathrm{d}r, \qquad \tilde{\bar{w}}_r = \frac{\partial \Lambda(\bar{\phi})}{\partial \bar{\phi}} - \bar{w}_{r,ave},$$

and move to a moving frame of reference, by writing:

$$\tilde{\bar{w}} = \bar{w} - 1, \qquad \xi = z - (1 + \bar{w}_{r,ave})t.$$

Further, we introduce $\varepsilon = \delta Pe/2$ and infer from (2.56) that as well as the advective timescale (captured in t), the mean concentration will also respond on the slow timescale: $T = \varepsilon t$. We do the latter by a multiple timescales approach, assuming that $\bar{\phi} = \bar{\phi}(t, T, r, \xi)$.

Equations (2.55) and (2.56) become, in the moving frame

$$0 = \frac{1}{r}\frac{\partial}{\partial r}(r\bar{u}) + \frac{\partial \tilde{\bar{w}}}{\partial \xi}, \tag{2.57}$$

$$\varepsilon \left[\frac{\partial \bar{\phi}}{\partial t} + \varepsilon \frac{\partial \bar{\phi}}{\partial T} + \bar{u}\frac{\partial \bar{\phi}}{\partial r} + \tilde{\bar{w}}\frac{\partial \bar{\phi}}{\partial \xi} + \tilde{\bar{w}}_r \frac{\partial \bar{\phi}}{\partial \xi} \right] = \frac{1}{r}\frac{\partial}{\partial r}(r D_d \frac{\partial \bar{\phi}}{\partial r}) + \frac{\varepsilon^2}{Pe^2}\frac{\partial}{\partial \xi}\left(D_d \frac{\partial \bar{\phi}}{\partial \xi} \right). \tag{2.58}$$

These are coupled with the following boundary/symmetry conditions

$$\frac{\partial \bar{\phi}}{\partial r} = 0 \quad \text{at} \quad r = 0,\ 1, \tag{2.59}$$

$$\bar{u} = 0 \quad \text{at} \quad r = 0,\ 1. \tag{2.60}$$

We now exploit the fact that $\varepsilon \ll 1$ to derive a leading order approximation to the behaviour of $\bar{\phi}$, using the following asymptotic expansion

$$\begin{aligned}
\bar{\phi}(t,T,r,\xi) &= \bar{\phi}_0(t,T,r,\xi) + \varepsilon\bar{\phi}_1(t,T,r,\xi) + \varepsilon^2\bar{\phi}_2(t,T,r,\xi) + \cdots, \\
\bar{u}(t,T,r,\xi) &= \bar{u}_0(t,T,r,\xi) + \varepsilon\bar{u}_1(t,T,r,\xi) + \varepsilon^2\bar{u}_2(t,T,r,\xi) + \cdots, \\
\tilde{\bar{w}}(t,T,r,\xi) &= \tilde{\bar{w}}_0(t,T,r,\xi) + \varepsilon\tilde{\bar{w}}_1(t,T,r,\xi) + \varepsilon^2\tilde{\bar{w}}_2(t,T,r,\xi) + \cdots.
\end{aligned}$$

Zero-th order problem:
At leading order we have:

$$
\begin{aligned}
0 &= \frac{1}{r}\frac{\partial}{\partial r}(r\bar{u}_0) + \frac{\partial \tilde{\bar{w}}_0}{\partial \xi}, && (2.61)\\
0 &= \frac{1}{r}\frac{\partial}{\partial r}(rD_{d,0}\frac{\partial \bar{\phi}_0}{\partial r}). && (2.62)\\
\frac{\partial \bar{\phi}_0}{\partial r} &= 0 \text{ at } r = 0, 1,
\end{aligned}
$$

where the additional subscripts mean that the expressions are expanded with respect to the leading order variables. From (2.62) we see that ϕ_0 has no $\hat{r}$-dependency. One consequence of this is that, since the relative velocity varies radially only via $\bar{\phi}$, we have that $\Lambda = \bar{\phi}(1-\bar{\phi})\bar{w}_r$ is also independent of r and hence:

$$\tilde{\bar{w}}_{r,0} = 0.$$

First order problem: At first order we have:

$$
\begin{aligned}
\frac{\partial \bar{\phi}_0}{\partial t} + \tilde{\bar{w}}_0\frac{\partial \bar{\phi}_0}{\partial \xi} &= \frac{1}{r}\frac{\partial}{\partial r}\left(rD_{d,0}\frac{\partial \bar{\phi}_1}{\partial r}\right), && (2.63)\\
\frac{\partial \bar{\phi}_1}{\partial r} &= 0 \text{ at } r = 0, 1.
\end{aligned}
$$

with all other terms vanishing since ϕ_0 has no $\hat{r}$-dependency. We then multiply by r and integrate (2.63) with respect to r over $[0, 1]$. The right-hand side vanishes due to the boundary conditions on ϕ_1. On the LHS, we find only: $\frac{\partial \bar{\phi}_0}{\partial t} = 0$, as $\tilde{\bar{w}}_0$ has zero average. It follows that at leading order $\bar{\phi}_0 = \bar{\phi}_0(T, \xi)$.

Returning to (2.63), we now find:

$$\bar{\phi}_1(t, T, r, \xi) = \bar{\phi}_1(t, T, 0, \xi) + \frac{\partial \bar{\phi}_0}{\partial \xi}(T, \xi)\psi(T, r, \xi), \qquad (2.64)$$

where

$$\psi(T,r,\xi) = \int_0^r \frac{1}{sD_{d0}} \left(\int_0^s y\tilde{\bar{w}}_0(T,y,\xi)\ \mathrm{d}y \right)\ \mathrm{d}s. \tag{2.65}$$

Second order problem: At $O(\varepsilon^2)$, we find that $\bar{\phi}_2$ satisfies:

$$\begin{aligned} \frac{\partial\bar{\phi}_0}{\partial T} + \frac{\partial\bar{\phi}_1}{\partial t} + \bar{u}_0\frac{\partial\bar{\phi}_1}{\partial r} + \tilde{\bar{w}}_0\frac{\partial\bar{\phi}_1}{\partial \xi} + \tilde{\bar{w}}_1\frac{\partial\bar{\phi}_0}{\partial \xi} + \tilde{\bar{w}}_{r,1}\frac{\partial\bar{\phi}_0}{\partial \xi} &= \frac{1}{r}\frac{\partial}{\partial r}\left(rD_{d,0}\frac{\partial\bar{\phi}_2}{\partial r} + rD_{d,1}\frac{\partial\bar{\phi}_1}{\partial r}\right) \\ &\quad + \frac{1}{Pe^2}\frac{\partial}{\partial\xi}\left(D_{d0}\frac{\partial\bar{\phi}_0}{\partial\xi}\right), \qquad (2.66) \\ \frac{\partial\bar{\phi}_2}{\partial r} &= 0 \text{ at } r = 0, 1. \end{aligned}$$

We multiply by $2r$ and integrate (2.66) with respect to r over $[0,1]$. We use (2.61) to combine the 3rd and 4th terms on the left hand side. After the integration, only the following terms are non-zero:

$$\frac{\partial\bar{\phi}_0}{\partial T} + \frac{\partial\bar{\phi}_1}{\partial t}(t,T,0,\xi) + \frac{\partial}{\partial\xi}\int_0^1 2r\bar{\phi}_1\tilde{\bar{w}}_0\ \mathrm{d}r = \frac{1}{Pe^2}\frac{\partial^2\bar{\phi}_0}{\partial\xi^2}.$$

Now we substitute for $\bar{\phi}_1$ and integrate by parts the third term:

$$\frac{\partial\bar{\phi}_0}{\partial T} + \frac{\partial\bar{\phi}_1}{\partial t}(t,T,0,\xi) = \frac{\partial}{\partial\xi}\left(\left[D_T + \frac{1}{Pe^2}\right]\frac{\partial\bar{\phi}_0}{\partial\xi}\right).$$

where D_T is the Taylor dispersion coefficient, given by:

$$D_T = 2\int_0^1 \frac{1}{sD_{d,0}}\left[\int_0^s y\tilde{\bar{w}}_0(T,y,\xi)\ \mathrm{d}y\right]^2\ \mathrm{d}s. \tag{2.67}$$

Note that the only term that depends on t is $\frac{\partial\bar{\phi}_1}{\partial t}(t,T,0,\xi)$. It is not hard to deduce that $\bar{\phi}_1(t,T,0,\xi) = A(T,\xi)t + B(T,\xi)$, so that the only bounded solution for $\bar{\phi}_1$ must have $A(T,\xi) = 0$.

Synopsis: the axial diffusion equation

Finally, this leads to the following diffusion equation for $\bar{\phi}_0(T,\xi)$:

$$\frac{\partial \bar{\phi}_0}{\partial T} = \frac{\partial}{\partial \xi}\left(\left[D_T + \frac{1}{Pe^2}\right]\frac{\partial \bar{\phi}_0}{\partial \xi}\right), \tag{2.68}$$

which can be written in the stationary frame of reference as:

$$\frac{\partial \bar{\phi}_0}{\partial T} + \frac{[1+\bar{w}_{r,ave}]}{\varepsilon}\frac{\partial \bar{\phi}_0}{\partial z} = \frac{\partial}{\partial z}\left(\left[D_T + \frac{1}{Pe^2}\right]\frac{\partial \bar{\phi}_0}{\partial z}\right), \tag{2.69}$$

or in conservative form and in terms of the fast time variable:

$$\frac{\partial \bar{\phi}_0}{\partial t} + \frac{\partial}{\partial z}F(\bar{\phi}_0) = \frac{\partial}{\partial z}\left(\varepsilon\left[D_T + \frac{1}{Pe^2}\right]\frac{\partial \bar{\phi}_0}{\partial z}\right): \quad F(\bar{\phi}_0) = \bar{\phi}_0[1+(1-\bar{\phi}_0)\bar{w}_r]. \tag{2.70}$$

To conclude, we rescaled the problem into dimensional form:

$$\frac{\partial \bar{\phi}_0}{\partial \hat{t}} + [\hat{U}_0 + \hat{\bar{w}}_{r,ave}]\frac{\partial \bar{\phi}_0}{\partial \hat{z}} = \frac{\partial}{\partial \hat{z}}\left(\hat{D}_{d,ave}\left[1 + Pe^2 D_T\right]\frac{\partial \bar{\phi}_0}{\partial \hat{z}}\right), \tag{2.71}$$

We observe that the leading order solids fraction diffuses relative to the mean motion of pumping plus the averaged settling. The diffusive spreading is amplified by Taylor dispersion, resulting in an effective axial diffusivity of $(1 + Pe^2 D_T)\hat{D}_{d,ave}$, where $\hat{D}_{d,ave}$ is the averaged particle dispersivity. The Taylor dispersion part of the axial diffusivity can be written in dimensional form as:

$$\begin{aligned}\hat{D}_T = Pe^2 D_T \hat{D}_{d,ave} &= \frac{\hat{R}^2\hat{U}_0^2}{\hat{D}_{d,ave}} 2\int_0^1 \frac{1}{sD_{d,0}}\left[\int_0^s y\tilde{\bar{w}}_0(T,y,\xi)\,\mathrm{d}y\right]^2 \mathrm{d}s \\ &= 2\int_0^{\hat{R}} \frac{1}{\hat{s}\hat{D}_{d,0}}\left[\frac{1}{\hat{R}}\int_0^{\hat{s}} \hat{y}(\hat{\bar{w}}_0 - \hat{U}_0)\,\mathrm{d}\hat{y}\right]^2 \mathrm{d}\hat{s}. \end{aligned} \tag{2.72}$$

2.2.2 Particle diffusivity models

To get an idea of the size of the axial diffusivity, we evaluate the Taylor dispersion coefficient for 3 sensible particle diffusivity models. In order to make comparisons between models, and because the dispersive part of the axial diffusivity is dominant, we adopt the same friction factor and velocity profile for each model.

The velocity profile is given dimensionally by (2.50) and dimensionlessly by (2.54). Both friction factor and velocity profile are derived in §2.1.4. We note that $\tilde{\bar{w}}_0$ is given by

$$\tilde{\bar{w}}_0 = \frac{\sqrt{0.5 f_f}}{\kappa_1}\left(\ln(1-r) + \frac{3}{2}\right). \tag{2.73}$$

and in the definition of D_T, we can evaluate:

$$\int_0^r y\tilde{\bar{w}}_0(T, y, \xi)\ \mathrm{d}y = -\frac{\sqrt{0.5 f_f}}{2\kappa_1}(1-r)\left(r + (1+r)\ln(1-r)\right). \tag{2.74}$$

Homogeneous slurry/Reynolds analogy approach

This approach treats the slurry as a fluid-solid mixture, modeled locally with an effective viscosity, and then applies Reynolds analogy. The mixture momentum balance along the pipe (2.23), is effectively:

$$\frac{\hat{r}}{2}\frac{\partial \hat{P}}{\partial \hat{z}} = \hat{\tau}_{rz} = \hat{\mu}_e \frac{\partial \hat{\bar{w}}}{\partial \hat{r}} \Rightarrow \hat{\mu}_e = -\frac{\hat{r}}{\hat{R}}\hat{\rho}(\hat{W}^*)^2\left[\frac{\partial \hat{\bar{w}}}{\partial \hat{r}}\right]^{-1}, \tag{2.75}$$

where $\hat{\mu}_e$ represents the effective viscosity. We apply Reynolds analogy to approximate the diffusivity coefficient of the particles, $\hat{D}_d$, which is assumed equivalent to that of the liquid in the mixture (i.e. we equate the diffusive transport of mass and momentum by the turbulent eddies). This leads to:

$$\hat{D}_d = \frac{\hat{\mu}_e}{\hat{\rho}} \approx -\frac{\hat{r}}{\hat{R}}(\hat{W}^*)^2\left[\frac{\partial \hat{\bar{w}}}{\partial \hat{r}}\right]^{-1} = \hat{R}\hat{W}^*\kappa_1 r(1-r) \tag{2.76}$$

Therefore, we find:

$$\hat{D}_{d,ave} = \frac{\hat{R}\hat{W}^*\kappa_1}{6} = \hat{R}\hat{U}_0\frac{\kappa_1\sqrt{0.5f_f}}{6} \tag{2.77}$$

$$D_{d,0} = 6r(1-r). \tag{2.78}$$

The Péclet number is evaluated as: $Pe = 6/(\kappa_1\sqrt{0.5f_f})$ and we compute:

$$D_T(\bar{\phi}_0) = \frac{f_f}{24\kappa_1^2}\int_0^1 \frac{(1-r)^2[r+(1+r)\ln(1-r)]^2}{r[r(1-r)]}\,\mathrm{d}r \approx 0.0851 f_f. \tag{2.79}$$

Finally, the dimensional total axial diffusivity is:

$$(1+Pe^2 D_T)\hat{D}_{d,ave} \approx [1+19.155]\hat{D}_{d,ave} \approx 0.95\hat{R}\hat{U}_0\sqrt{f_f} \tag{2.80}$$

Note that approximately 95% of the total axial diffusivity is due to Taylor dispersion.

Walton

In [48] Walton uses dimensional analysis arguments to arrive at an assumed functional form of the particle diffusivity closure relation:

$$\hat{D}_d = \hat{U}_0\hat{R}\bar{\epsilon}_{p0}: \qquad \bar{\epsilon}_{p0} \propto \delta^{a_1}Re^{a_2}. \tag{2.81}$$

The coefficients in the above expression are fitted to existing experimental data collected by [30]. Note that there is no radial dependence of $\hat{D}_d$.

For simplicity we take the same approach. However as discussed above, we substitute our friction factor closure from equation (2.38), in order to include both non-Newtonian and solid volume fraction effects. This leads to the following expression for the particle diffusivity

$$\hat{D}_d = \hat{D}_{d,ave} = 2\hat{U}_0\hat{R}\sqrt{0.5f_f}\frac{0.014\delta_p^{0.96}Re^{0.33}}{\sqrt{0.5\times 0.079Re^{-0.25}}}. \tag{2.82}$$

It follows that

$$D_{d,0} = 1, \tag{2.83}$$

$$Pe = \frac{1}{2\sqrt{0.5 f_f}} \frac{\sqrt{0.5 \times 0.079 Re^{-0.25}}}{0.014 \delta_p^{0.96} Re^{0.33}}, \tag{2.84}$$

$$D_T(\phi_0) = \frac{f_f}{4\kappa_1^2} \int_0^1 \frac{\left[(1-r)\left(r + (1+r)\ln(1-r)\right)\right]^2}{r} \, \mathrm{d}r \approx 0.1703 f_f \tag{2.85}$$

Finally, the dimensional axial diffusivity is:

$$(1 + Pe^2 D_T)\hat{D}_{d,ave} \approx [1 + 17.16 Re^{-0.91} \delta_p^{-1.92}]\hat{D}_{d,ave}, \tag{2.86}$$

which shows a strong dependency on particle diameter ratio and bulk Reynolds number.

Eskin

Eskin's approach [17] is in some ways similar to Walton [48] , although the rationale is different. In [17] the following model for $\hat{D}_{d,ave}$ is derived.

$$\hat{D}_{d,ave} = 2\hat{U}_0 \hat{R} \times 0.292 \delta_p^{0.32} f_f^{2/3} \left(1 + \frac{Re_p}{18} \frac{\hat{U}_0}{\hat{\bar{w}}_{r,0}} s \delta_p \frac{C_{D0}}{C_D}\right) \tag{2.87}$$

The second term above is included to account for potential particle relaxation effects in flows that are inertial on the particle scale. Again no variation with

r is considered and hence we find the following expressions:

$$D_{d,0} = 1, \tag{2.88}$$

$$Pe = \frac{1}{0.584\delta_p^{0.32} f_f^{2/3}} \frac{1}{1 + \frac{Re_p}{18} \frac{\hat{U}_0}{\hat{\bar{w}}_{r,0}} s\delta_p \frac{C_{D0}}{C_D}}, \tag{2.89}$$

$$D_T(\phi_0) = \frac{f_f}{4\kappa_1^2} \int_0^1 \frac{\left[(1-r)\left(r + (1+r)\ln(1-r)\right)\right]^2}{r} \, \mathrm{d}r \approx 0.1703 f_f \tag{2.90}$$

The dimensional axial diffusivity is:

$$(1 + Pe^2 D_T)\hat{D}_{d,ave} \approx \left[1 + \frac{4.58\delta_p^{-0.64} f_f^{-1/3}}{\left[1 + \frac{Re_p}{18} \frac{\hat{U}_0}{\hat{\bar{w}}_{r,0}} s\delta_p \frac{C_{D0}}{C_D}\right]^2}\right] \hat{D}_{d,ave}, \tag{2.91}$$

Comparison of the particle diffusivity models

Figure 2.6 shows variations in Pe for the three particle diffusivity models outlined above. We plot Pe against both $(\hat{U}_0, \bar{\phi})$ and $(\hat{d}_p, \bar{\phi})$. We note that the range of Pe number is similar for both the Homogeneous slurry/Reynolds analogy approach and Eskin's approach [17]. However, the homogeneous slurry approach has no sensitivity to particle size and variations with $\hat{U}_0$ at lower concentrations $\bar{\phi}$ differ from Eskin's model. Pe is a decreasing function of particle size in both Walton's approach [48] and Eskin's approach [17]. Which implies that particle diffusivity increases with particle size. The Homogeneous slurry/Reynolds analogy approach does not depend on particle size.

Figure 2.7 shows $D_T Pe^2$ for Walton's approach [48] and Eskin's approach [17]. It can be seen that Taylor dispersion is the main mechanism for axial diffusion of the mean solids fraction. Eskin's approach [17] gives similar range for $D_T Pe^2$ as does the Homogeneous slurry/Reynolds analogy approach, which we have omitted for brevity. In general we can see that for large parameter ranges over 95% of the axial dispersion is due to Taylor dispersion, (see (2.91)).

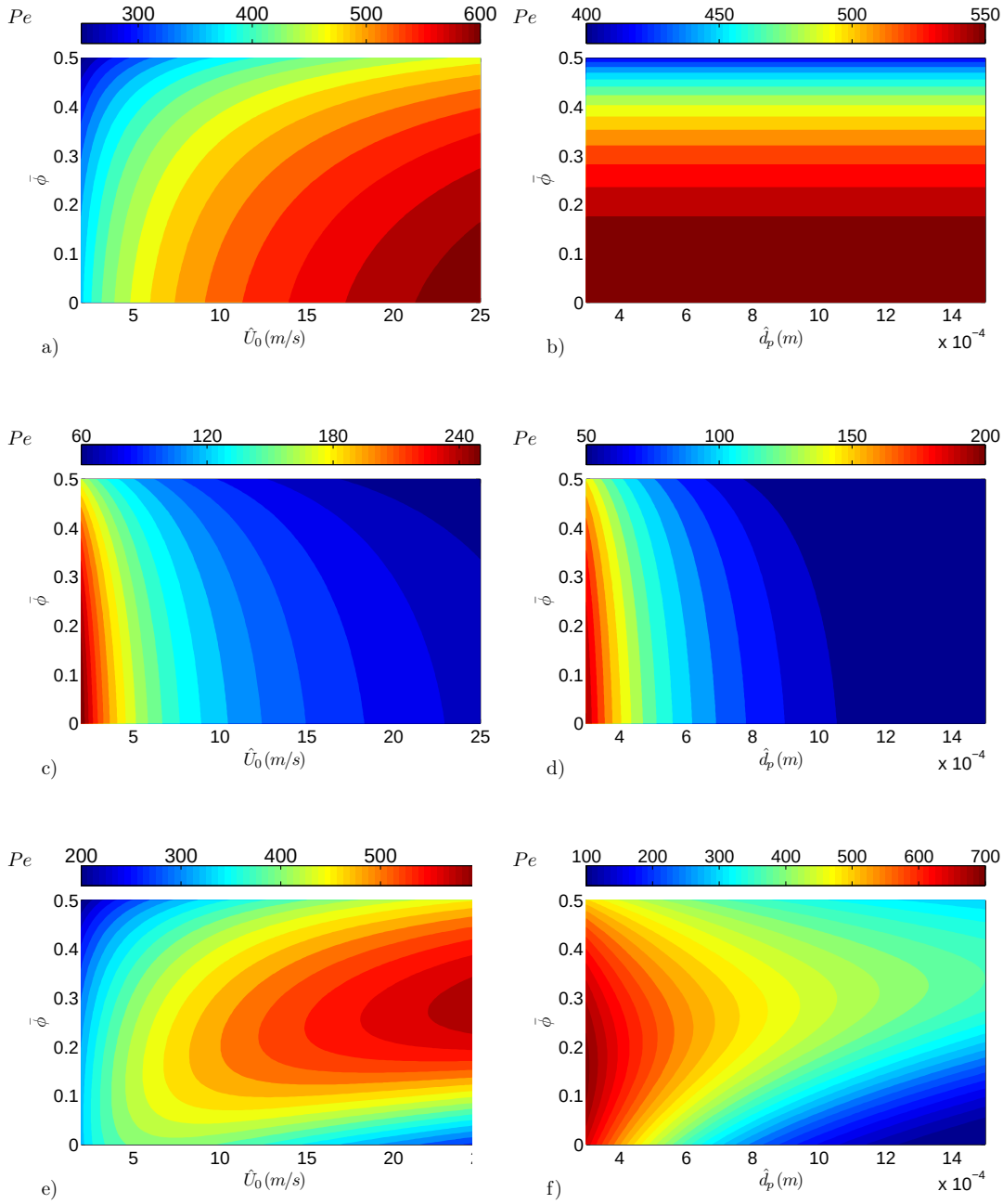

Figure 2.6: Variations in Pe for the different particle diffusivity models: a) & b) Homogeneous slurry/Reynolds analogy approach; c) & d) Walton's approach [48]; e) & f) Eskin's approach [17]. For all figures, we have $n = 0.5$, $\hat{K}_0 = 0.1$Pa.s^n, $\hat{\tau}_{Y0} = 1$Pa, $s = 2.65$, $\hat{D} = 62$mm. For a), c) and e) $\delta_p = 0.01$; for b), d) and f) $\hat{U}_0 = 15m/s$.

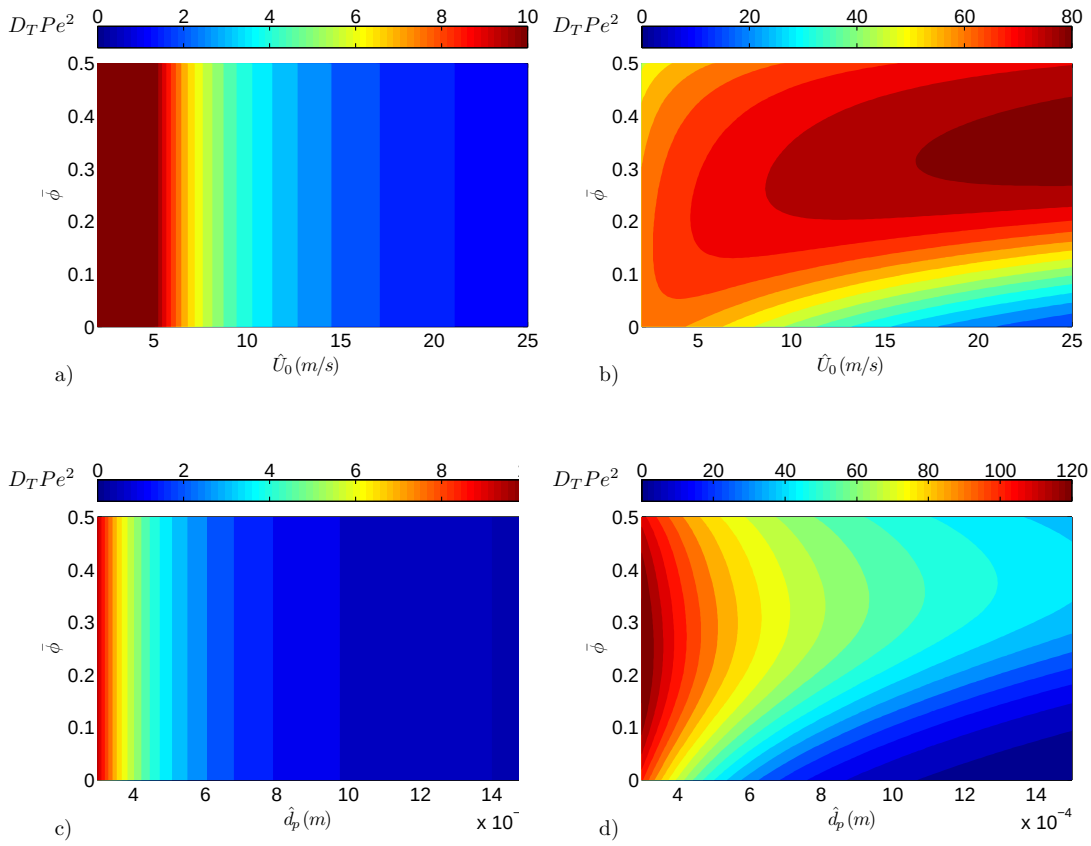

Figure 2.7: Variations in $D_T Pe^2$ for the different particle diffusivity models; a) & c) Walton's approach [48]; b) & d) Eskin's approach [17]. For all figures, we have $n = 0.5$, $\hat{K}_0 = 0.1$Pa.s^n, $\hat{\tau}_{Y0} = 1$Pa, $s = 2.65$, $\hat{D} = 62$mm. For a) and b) $\delta_p = 0.01$; for c) and d) $\hat{U}_0 = 15m/s$.

We need to be cautious about our interpretations of predictions using Walton's or Eskin's models, which are included mainly for comparison. We see that the majority of the solids transport is governed by axial dispersion, which is related to the the velocity profile. Here we have used the same velocity profile for all models. However implicitly, the semi-empirical relations that define the turbulent particle dispersivity in terms of a friction factor may be based on different interpretations of the slurry velocity field.

2.2.3 Slug spreading estimates

If we observe the general form of (2.71) and consider the behaviour of a slug of proppant pumped down the pipe at mean speed $\hat{U}_0$, we see that there are two main mechanisms that lead to spreading of the slug: (i) slip of the solids phase due to settling, ahead of the mean flow; (ii) diffusion of the slug, primarily through Taylor dispersion. Denoting the length of well by $\hat{L}$ the transit time to reach the bottom of the well is $\hat{L}/\hat{U}_0$.

(i) The effect of settling is captured by the term $\hat{\bar{w}}_{r,ave}$. The leading order concentration is uniform across the pipe, so this term is simply:

$$\hat{\bar{w}}_{r,ave} = \frac{\partial}{\partial \bar{\phi}}[\bar{\phi}(1-\bar{\phi})\hat{\bar{w}}_r]_{\bar{\phi}=\bar{\phi}_0}.$$

Spreading of the front of the slug due to settling occurs when $\hat{\bar{w}}_{r,ave}$ decreases with $\bar{\phi}_0$, since the lower concentrations are then advected furthest. This situation is usually the case, since the settling velocity decreases with $\bar{\phi}_0$. Similarly, at the rear of a slug we may expect to see some sharpening of the front.

We can estimate the difference in speeds of settling at the front of the slug, by

$$\hat{\bar{w}}_{r,ave}(\bar{\phi}_0 = 0) - \hat{\bar{w}}_{r,ave}(\bar{\phi}_{in}) \approx \hat{\bar{w}}_{r,ave}(\bar{\phi}_0 = 0) = \hat{\bar{w}}_r(\bar{\phi}_0 = 0),$$

i.e. this assumes that the settling speed at the input concentration $\bar{\phi}_{in}$ is relatively small. Consequently, a length estimate, for the effect of spreading due to settling is

$$L_{mix1} = \frac{\hat{L}_{mix1}}{\hat{L}} = \frac{1}{\hat{L}}\left[\frac{\hat{L}}{\hat{U}_0}\hat{\bar{w}}_r(\bar{\phi}_0 = 0)\right] = \frac{\hat{\bar{w}}_r(\bar{\phi}_0 = 0)}{\hat{U}_0}, \tag{2.92}$$

which we have expressed as a ratio of the length of the pipe.

(ii) We can also estimate the net effect of diffusivity on spreading the slug. From the Taylor dispersivity D_T and the range of $\bar{\phi}_0$ pumped into the well, we can estimate a representative dispersivity $D_{T,0}$, (e.g. either the maximum or an average value). A diffusive length-scale is given by

$$\hat{L}_{mix2} = \sqrt{8\hat{D}_{d,ave}\frac{\hat{L}}{\hat{U}_0}\left[1 + Pe^2 D_{T,0}\right]},$$

or a ratio of the pipe length:

$$L_{mix2} = \frac{\hat{L}_{mix2}}{\hat{L}} = \sqrt{8\frac{\hat{D}_{d,ave}}{\hat{L}\hat{U}_0}\left[1 + Pe^2 D_{T,0}\right]} = 2\delta^{1/2}\sqrt{\frac{1}{Pe} + PeD_{T,0}}. \tag{2.93}$$

In Figs. 2.4-2.5 we have explored the variation in $\hat{\bar{w}}_r/\hat{U}_0$, which characterizes L_{mix1}. Although generally small the length L_{mix1} is independent of the pipe length $\hat{L}$. On the other hand L_{mix2} depends on the pipe aspect ratio, (proportionate to $\delta^{1/2}$). The two estimates are plotted in Fig. 2.8. Although for many parameter ranges the diffusive effect will dominate, in any sufficiently long pipe L_{mix1} can be significant with respect to L_{mix2}. This type of estimate is perhaps the easiest to use for design purposes and note that it could be more appropriate for application to scale with the distance between slugs, rather the the pipe length, in assessing whether spreading effects are significant.

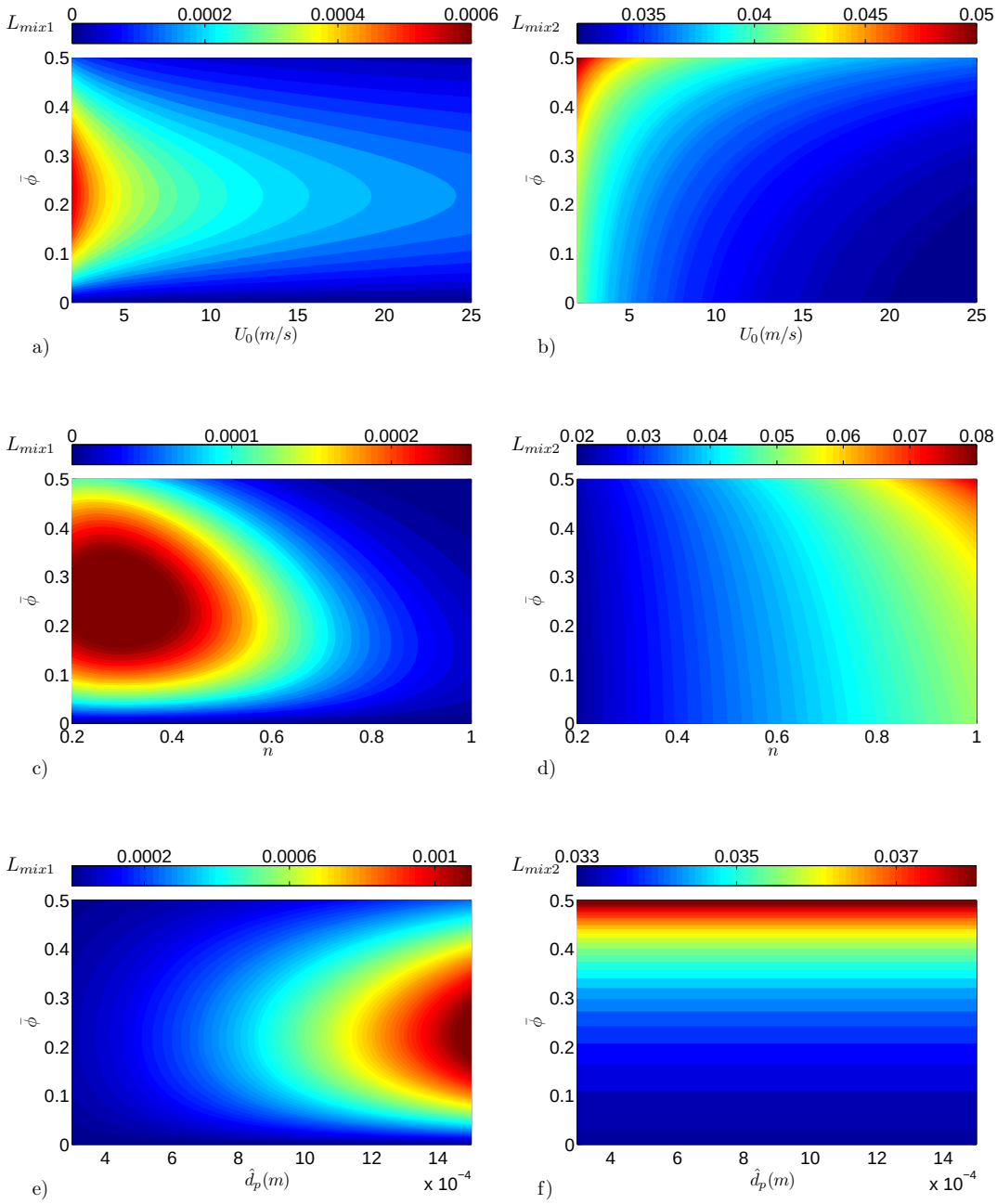

Figure 2.8: Estimates of the lengths that a proppant slug will spread, based on particle settling (slip), L_{mix1}, and particle diffusion, L_{mix2}. Both length scales are made dimensionless with the length of the pipe $\hat{L}$. Parameters are $\hat{K}_0 = 0.1$Pa.s^n, $\hat{\tau}_{Y0} = 1$Pa, $s = 2.65$, $\hat{D} = 62$mm, $\delta = 0.001$: a) and b) $\delta_p = 0.01$, $n = 0.5$; c) and d) $\hat{U}_0 = 15$ m/s, $\delta_p = 0.01$; e) and f) $\hat{U}_0 = 15$ m/s, $n = 0.5$.

Chapter 3

Results

In this chapter, we present results based on the numerical solution of (2.70). Here, we drop subscript 0 for simplicity. In general, we seek for an algorithm to solve the following transport equation that was introduced in chapter 1.

$$\frac{\partial \bar{\phi}}{\partial t} + \frac{\partial F(\bar{\phi})}{\partial z} = \frac{\partial}{\partial z}[D(\bar{\phi})\frac{\partial \bar{\phi}}{\partial z}] \tag{3.1}$$

The challenge in solving this type of equation is that both advective slip and diffusive terms are relatively small. The main transport mechanism is clearly advection at the mean speed and in capturing this numerically we induce unwanted numerical errors (typically diffusive and/or dispersive). Some care is needed in ensuring that the numerical errors do not mask the physical effects. Therefore, in the first part of this section we outline the numerical algorithm and present test results only. Thereafter, sample physical results are presented of relevance to slug dispersion.

3.1 Algorithm development

We deal first separately with the advective component in §3.1.1 and the diffusive component in §3.1.2, before combining the methods to solve (2.70) in §3.1.3.

3.1.1 Advection equation

We want to solve the following advection problem

$$\bar{\phi}_t + F(\bar{\phi})_z = 0 \tag{3.2}$$

Adopting a finite volume approach implies that we should study numerical methods of the form

$$\bar{\phi}_i^{n+1} = \bar{\phi}_i^n - \frac{\Delta t}{\Delta z}(F_{i+\frac{1}{2}}^n - F_{i-\frac{1}{2}}^n), \tag{3.3}$$

where $\bar{\phi}_i^n$ and $\bar{\phi}_i^{n+1}$ are the averaged value of the i-th cell at time t_n and t_{n+1} respectively. Here, $F_{i\pm\frac{1}{2}}$ is some approximation to the average flux along $z = z_{i\pm\frac{1}{2}}$:

$$F_{i+\frac{1}{2}}^n \approx \frac{1}{\Delta t}\int_{t_n}^{t_{n+1}} F(\bar{\phi}(z_{i+\frac{1}{2}}, t))\ \mathrm{d}t. \tag{3.4}$$

We use Godunov method (see [23]) to obtain an explicit formula for the numerical flux (3.4) as follow

$$F_{i+\frac{1}{2}}^n = F(\bar{\phi}_i^n, \bar{\phi}_i^{n+1}) = \begin{cases} \min\limits_{\bar{\phi}_i^n < \varphi < \bar{\phi}_{i+1}^n} F(\varphi) & \bar{\phi}_i^n \leq \bar{\phi}_{i+1}^n, \\ \max\limits_{\bar{\phi}_{i+1}^n < \varphi < \bar{\phi}_i^n} F(\varphi) & \bar{\phi}_{i+1}^n \leq \bar{\phi}_i^n. \end{cases} \tag{3.5}$$

This formula is valid also for non-convex flux functions. Implementing the Godunov scheme (3.5) is straightforward. The temporal update (3.3) is simple to compute as it is explicit, but computing the fluxes can be complicated, since an optimization problem has to be solved locally (see above). If the flux function F has a single minimum at the point ω and no local maxima, then the formula (3.5) can be simplified to

$$F_{i+\frac{1}{2}}^n = F(\bar{\phi}_i^n, \bar{\phi}_i^{n+1}) = \max\left(F(\max(\bar{\phi}_i^n, \omega)), F(\min(\bar{\phi}_{i+1}^n, \omega))\right). \tag{3.6}$$

If the cell averages are selected as a piecewise constant function in (3.3), this is known to result in an overall first order accuracy of the Godunov-type schemes. However, given the cell averages $\bar{\phi}_i^n$ at time t_n, we can instead reconstruct linear functions in each cell, which leads to a second-order accurate solution. We denote the piecewise linear function in the cell i_{th} cell as $p_i(z)$, which takes the form

$$p_i(z) \quad = \quad \bar{\phi}_i^n + \sigma_i^n (z - z_i). \tag{3.7}$$

where σ_i^n is a parameter that determines the slope in cell Ω_i. The proper choice of σ_i^n satisfies the Total Variation Diminishing (TVD) property. For example the following so-called *minmod* limiter is TVD

$$\sigma_i^n \quad = \quad minmod\left(\frac{\bar{\phi}_{i+1}^n - \bar{\phi}_i^n}{\Delta z}, \frac{\bar{\phi}_i^n - \bar{\phi}_{i-1}^n}{\Delta z}\right), \tag{3.8}$$

where the *minmod* function is defined as

$$minmod(a,b) = \begin{cases} sign(a)\min(|a|,|b|) & sign(a) = sign(b), \\ \\ 0 & otherwise. \end{cases} \tag{3.9}$$

A wide variety of other slope limiters such as Superbee, Monotonized central-difference (MC), Van Leer and etc, have also been proposed in the literature, (see e.g. [23] for an overview).

Despite the second-order accuracy of the piecewise linear reconstruction (3.7), the first-order temporal accuracy leads to an overall first-order accuracy, which negates the purpose of using a piecewise linear reconstruction. Therefore, instead, we implement a second-order time stepping method. We use Runge-Kutta methods that preserve the TVD property. Such methods are termed *Strong Stability Preserving* (SSP) Runge-Kutta methods. In particu-

lar, we use the following second-order SSP-Runge-Kutta method

$$\begin{aligned}\bar{\phi}^{*} &= \bar{\phi}^{n} + \Delta t L(\bar{\phi}^{n}) \\ \bar{\phi}^{**} &= \bar{\phi}^{*} + \Delta t L(\bar{\phi}^{*}) \\ \bar{\phi}^{n+1} &= \frac{1}{2}(\bar{\phi}^{n} + \bar{\phi}^{**}),\end{aligned} \tag{3.10}$$

where, the operator L denotes any operator acting pointwise on $\bar{\phi}$, which here takes the form:

$$L(\bar{\phi}(t))_i = -\frac{1}{\Delta z}(F_{i+\frac{1}{2}}(t) - F_{i-\frac{1}{2}}(t)). \tag{3.11}$$

In summary, with all the above ingredients in place, we can state the algorithm for computing with a second-order scheme. Given cell averages $\bar{\phi}_i$ at time level t_n , we need to perform the following steps:

Step 1 (Reconstruction): $\bar{\phi}_i$, reconstruct the averages to obtain the piecewise linear function (3.7). Any nonoscillatory slope limiter like the *minmod* (3.8), Superbee or the MC limiter can be used. Note that we only require the edge values $\bar{\phi}_i$ at each cell.

Step 2 (Flux evaluation): Given the edge values $\bar{\phi}_i$ at each cell, we plug these values into the numerical flux (3.5).

Step 3 (Time stepping): For second-order schemes, we use the second-order SSP Runge-Kutta method (3.10). As this method consists of 2 stages, steps 1 and 2 must be applied to each stage (e.g., $\bar{\phi}^n$ and $\bar{\phi}^*$).

The time step Δt in (3.10) is determined by a *CFL* condition of the form

$$\max_i |\frac{\partial F(\bar{\boldsymbol{\phi}}_i^n)}{\partial \bar{\boldsymbol{\phi}}}| \frac{\Delta t}{\Delta z} \leq CFL. \tag{3.12}$$

The above second-order high resolution scheme is TVD as all the three ingredients are constructed to ensure this property.

As well as the second-order Godunov-type schemes, we have also implemented a second-order extension of the staggered Lax-Friedrichs scheme, as introduced by Nessyahu & Tadmor [29], (commonly called the NT scheme). This scheme is one of the simplest possible examples of second-order central schemes and slightly faster compared to the second-order Godunov-type schemes. Generally we have found better results using the NT scheme. As a test, we have used the NT scheme with different limiters to solve the linear (constant speed) advection problem for initial data consisting of a combination of a smooth, squared cosine wave and double step function. Note that for the fracturing problem the main advective component is a constant velocity, with smaller settling velocity contribution. With the scaling used in deriving (2.70), it is clear that to simulate the physical process we will advect pulses for a unit time and distance, hence the relevance of this example. In order to examine longer time attenuation we impose periodic boundary condition on our unit domain.

Figures 3.1 and 3.2 show the numerical solution after 9.5 and 10 time units respectively. We can see that in all cases the results are very robust with an insignificant amount of numerical diffusion. The exact solution simply advects the intial condition (shown) at unit speed, so that Fig. 3.2 in fact compares the exact and numerical solutions at $t = 10$. Of the 4 limiters tested, the Superbee limiter appears to resolve the discontinuities better.

3.1.2 Diffusion equation

In this section, we explain the numerical method for the diffusive component, i.e. we solve the following quasi-linear parabolic equation.

$$\bar{\phi}_t = [D(\bar{\phi})\bar{\phi}_z]_z. \tag{3.13}$$

There are many methods used for such equations, which are not difficult to solve. Here, we use the CPC method of [25] which is a simplified version

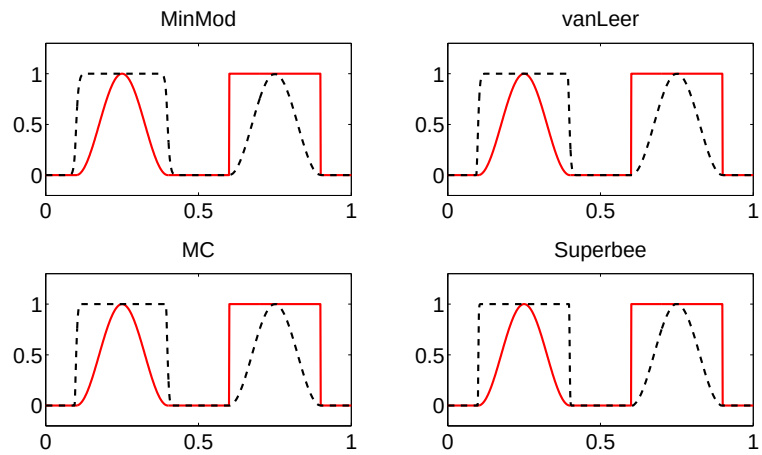

Figure 3.1: Solution of the linear (constant speed) advection problem in a periodic domain with unit length by the NT scheme at $t = 9.5$ (i.e. after 9.5 time periods), $CFL = 0.4, \Delta z = 0.001$. Solid line: initial condition; dashed line: numerical solution.

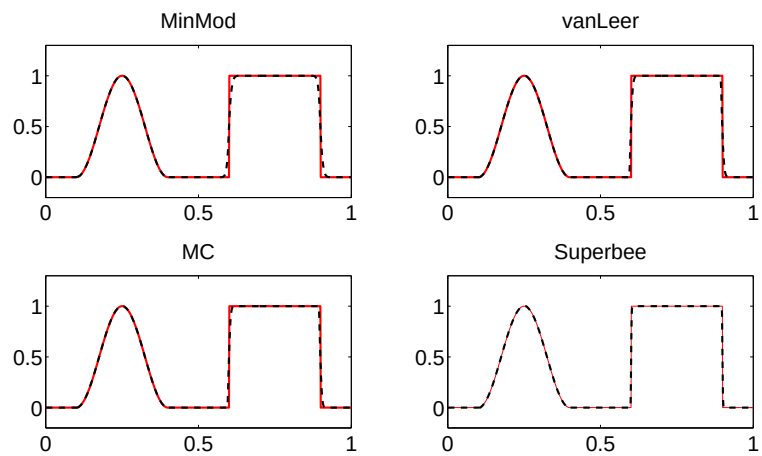

Figure 3.2: Solution of the linear (constant speed) advection problem in a periodic domain with unit length by the NT scheme at $t = 10$ (i.e. after 10 time periods), $CFL = 0.4, \Delta z = 0.001$. Solid line: initial condition; dashed line: numerical solution.

of a Newton Predictor-Corrector (NPC) scheme. This method has a second-order convergence in space. Convergence in time direction is slightly less than second-order (i.e. $O(\Delta t^{2-\epsilon})$, for some small $\epsilon > 0$), but the method is simple to implement and stable.

The discretization of (3.13) consists of two stages both of which lead to a system of linear algebraic equation, that can be solved by a simple tri-diagonal matrix algorithm in favor of a more costly matrix inversion.

$$\frac{2}{\Delta t}(\bar{\phi}_i^* - \bar{\phi}_i^n) = \frac{1}{(\Delta z)^2}\nabla_z \left\{ D(z_{i+\frac{1}{2}}, \frac{1}{2}(\bar{\phi}_i^n + \bar{\phi}_{i+1}^n))\Delta_z \bar{\phi}_i^* \right\} \tag{3.14}$$

$$\frac{1}{\Delta t}(\bar{\phi}_i^{n+1} - \bar{\phi}_i^n) = \frac{1}{2(\Delta z)^2}\nabla_z \left\{ D(z_{i+\frac{1}{2}}, \frac{1}{2}(\bar{\phi}_i^* + \bar{\phi}_{i+1}^*))\Delta_z (\bar{\phi}_i^n + \bar{\phi}_i^{n+1}) \right\}. \tag{3.15}$$

Here ∇_z and Δ_z are backward and forward differencing operators respectively. To test this scheme we consider the following three examples.

Example 1:

$$\bar{\phi}_t = [D(\bar{\phi})\bar{\phi}_z]_z, \quad 0 \le z \le 1 \qquad 0 \le t \le 2$$
$$D(z, \bar{\phi}) = \exp(z)(2z + \exp(-z))[1 + (\exp(-z) - 2)/\bar{\phi}]. \tag{3.16}$$

Here the exact solution is $\bar{\phi} = (1+\exp(t))(2+\exp(-z))$. We take boundary and initial conditions consistent with the given exact solution and compare the two solutions at successive times. Figure 3.3a shows that the CPC method accurately approximates a well behaved solution to a parabolic equation with non constant diffusivity coefficient. Although the fracturing problem is quasilinear, the nonlinearity merely results in a bounded variation of the axial diffusivity along the pipe.

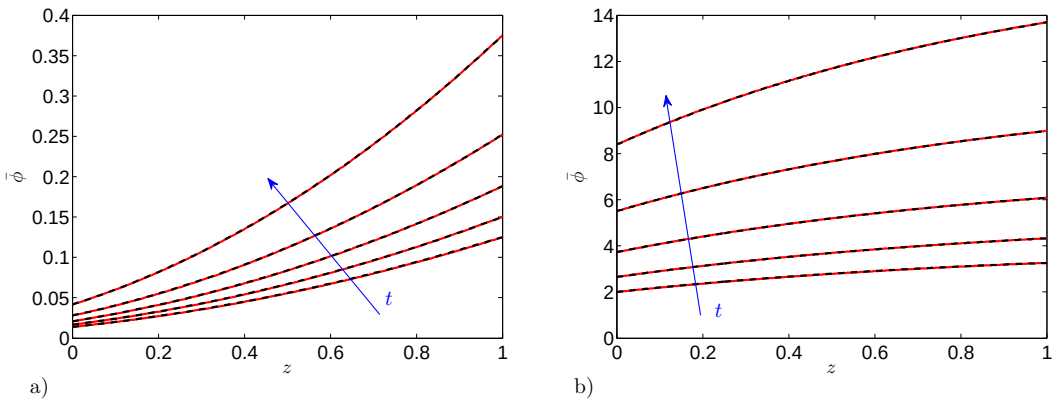

Figure 3.3: Exact (solid line) and numerical solution (dashed line) of diffusion equation for (a) example 1 and (b) example 2 at $t = 0,\ 0.5,\ 1.,\ 1.5,\ 2,\ \Delta t = 0.005$ & $\Delta z = 0.005$.

Example 2:

$$\bar{\phi}_t = [D(\bar{\phi})\bar{\phi}_z]_z,\ 0 \le z \le 1,\ 0 \le t \le 2\ \ D(z, \bar{\phi}) = \bar{\phi}. \tag{3.17}$$

Here the exact solution is $\bar{\phi} = (z + 0.5)^2/(18 - 3t)$. This example has a finite time blow-up and is used to investigate how well the CPC scheme behaves for a quasilinear equation with a discontinuity in time. Figure 3.3b shows the results for this case, again showing a good comparison with the analytical solution.

Example 3:

$$\bar{\phi}_t = [D(\bar{\phi})\bar{\phi}_z]_z,\ \ -4 \le z \le 4,\ 0 \le t \le 20\ \ D(z, \bar{\phi}) = 0.01 \tag{3.18}$$

The initial condition is a unit square wave of length 2 centered at the origin. We take no flux boundary conditions at the end points of our finite domain. On an infinite domain, the exact solution is $\bar{\phi} = 0.5[\mathrm{erf}(z+1)/\sqrt{4Dt} - \mathrm{erf}(z -$

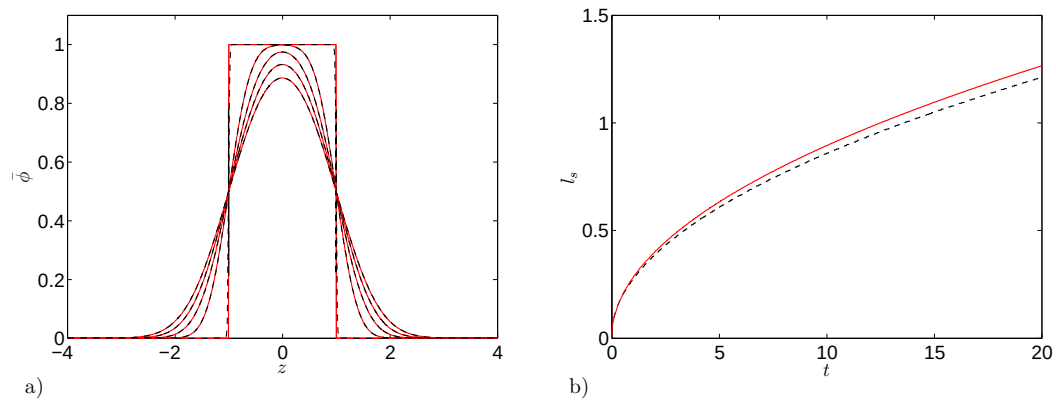

Figure 3.4: (a) Exact (solid line) and numerical solution (dashed line) of diffusion equation for example 3 at different time. (b) (dashed line) shows the computed spreading of the front and (solid line) shows the approximation $l_s = \sqrt{8Dt}$.

$1)/\sqrt{4Dt}]$. This example mimics the diffusive behavior of the fracturing problem, in a moving frame of reference. The aim however is to understand what is the proper characteristic length-scale for diffusion.

Note that we have approximated the diffusive spreading length-scale using the estimate $\sqrt{8Dt}$, earlier. The coefficient value 8 is derived from the analytical solution by requiring that the value of $\bar{\phi}$ in the domain be $\gtrsim 2\%$ of the maximum initial $\bar{\phi}$. Figure 3.4a shows the accuracy of the CPC scheme in approximating the spreading of a pulse. Figure 3.4b compares the estimate $\sqrt{8Dt}$ against a numerical approximation which computes the 2% limit from the numerical solution. We can see that the error is reasonable for times of $O(1)$, which is what is required for the fracturing process. Note that there are a number of different error sources here: (i) the coefficient 8 is not precise for the analytical solution; (ii) effects of the finite domain; (iii) numerical errors attributable to the scheme used.

3.1.3 Advection-Diffusion equation

Let's first consider the numerical solution to an advection-diffusion problem of the form

$$\bar{\phi}_t + F(\bar{\phi})_z = D\bar{\phi}_{zz}. \tag{3.19}$$

One standard approach for solving (3.19) is to use a fractional-step or operator-splitting method, in which we solve the following two simpler problem

$$\bar{\phi}_t + F(\bar{\phi})_z = 0 \tag{3.20}$$

$$\bar{\phi}_t = D\bar{\phi}_{zz} \tag{3.21}$$

Algorithmically, we start with initial data $\bar{\phi}_i^n$ to obtain the intermediate value $\bar{\phi}_i^*$ from (3.20), then we take $\bar{\phi}_i^*$ to obtain $\bar{\phi}_i^{n+1}$ from (3.21). This scheme is almost second-order accurate and we refer readers to [23] for a discussion on the splitting error and order of accuracy of such methods.

The splitting step (3.20) allows us to use second-order the method explained in §3.1.1 for the advection part without change. We also implement the scheme in §3.1.2 to take account of the diffusive part. As a test example, in Fig. 3.5 we show results of a constant speed linear advection and constant diffusion problem, comparing the numerical solution with the exact solution (from an infinite domain). The exact and numerical solutions are in a very good agreement.

3.2 Physical results

Finally we show some numerical results, solving (2.70) and showing the evolution of proppant pulses (slugs) for fracturing parameters. Figure 3.6a shows how an initial slug of proppant advects along the pipe in the absence of diffusion. Over the length of pipe considered, the spreading length due to slip

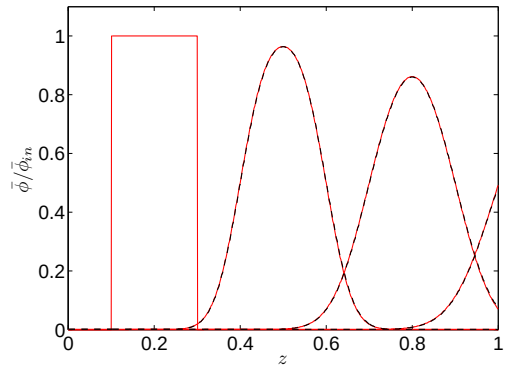

Figure 3.5: Exact (solid line) and numerical solution (dashed line) of the linear (constant coefficient) advection-diffusion equation at different times; parameters: $D = 0.3831, CFL = 0.4, dz = 0.001$.

of particles is clearly insignificant. We include the diffusion of solid particles in Fig. 3.6b, which appears to be the dominant spreading process for the parameters considered (a relatively short pipe and low Re). For the same basic parameters, Fig. 3.7b shows the interaction of two initially separate pulses due to diffusion.

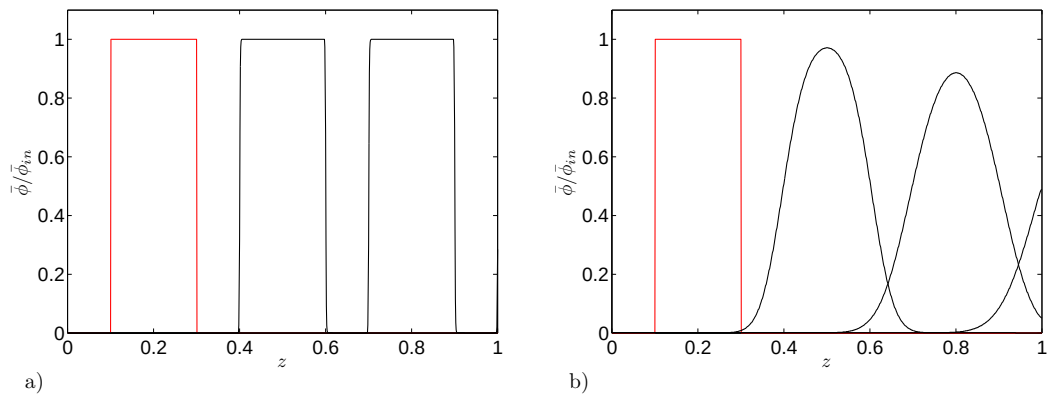

Figure 3.6: The evolution of a square wave at different time under transport equation (2.70) (a) excluding the diffusion part (b) including the diffusion part. Here, we have $Re = 3100, B = 0.62, Fr = 5, s = 2.65, \delta = 0.01, \delta_p = 0.01, \bar{\phi}_{in} = 40\%, n = 1$.

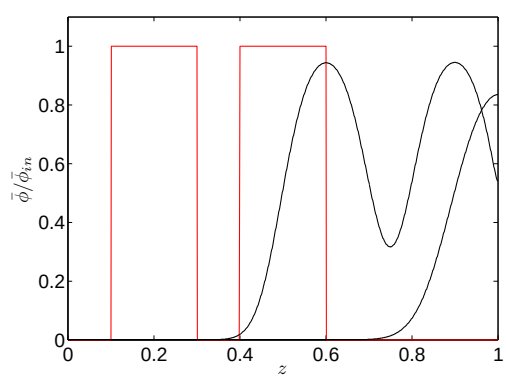

Figure 3.7: The interaction of two square waves transporting with equation (2.70) at different time. Here, we have $Re = 3100, B = 0.62, Fr = 5, s = 2.65, \delta = 0.01, \delta_p = 0.01, \bar{\phi}_{in} = 40\%, n = 1$.

Still solving (2.70), but moving now to a set of process parameters in a range given in Table 1.1 and Table 1.2, we show the effects of diffusion on a sequence of pulsed proppant slugs in Fig. 3.8. The pattern of pulse length (and interval between pulses) is more characteristic of fracturing process than the previous examples. We see that for these particular parameters the pulses remain quite square as they travel down the pipe. The last image however zooms in to a frontal region (here a backwards step) which reveals that the transitions between pulses are smooth.

As second example is shown in Fig. 3.9 for a typical set of fracturing parameters (i.e. the parameters about which we have varied the dimensionless groups previously). As pulse duration we have taken $\Delta t = 0.15$ and have taken an interval $\Delta t = 0.15$ between pulses. Although the pulses remain distinct, there is considerable rounding of the step discontinuities by the time the pulses attain the bottom of the pipe. Although there is no interaction at present, reducing the time interval between pulses would soon result in interaction.

To illustrate that pulse interaction can occur relatively easily, we have repeated the computation of Fig. 3.9, but with double the frequency of pulses (hence halving both the pulse duration and the time interval between pulses). Figure 3.10 shows the results of this change, which results in a modest amount of interaction by the end of the pipe.

The effects of pipe length are shown in Fig. 3.11 which follows the same parameters as Fig. 3.9, but with a pipe length 3 times as long ($\delta = 0.00033$). We have kept the dimensionless frequency of pulses the same (although arguably this should also have increased). We see that the pulses are interacting by the end of the pipe and the last image in Fig. 3.11 zooms into the pulses at the last time of the snapshot. We can see that as well as interacting the pulses are not completely symmetric. This may be due to the settling effect as discussed earlier.

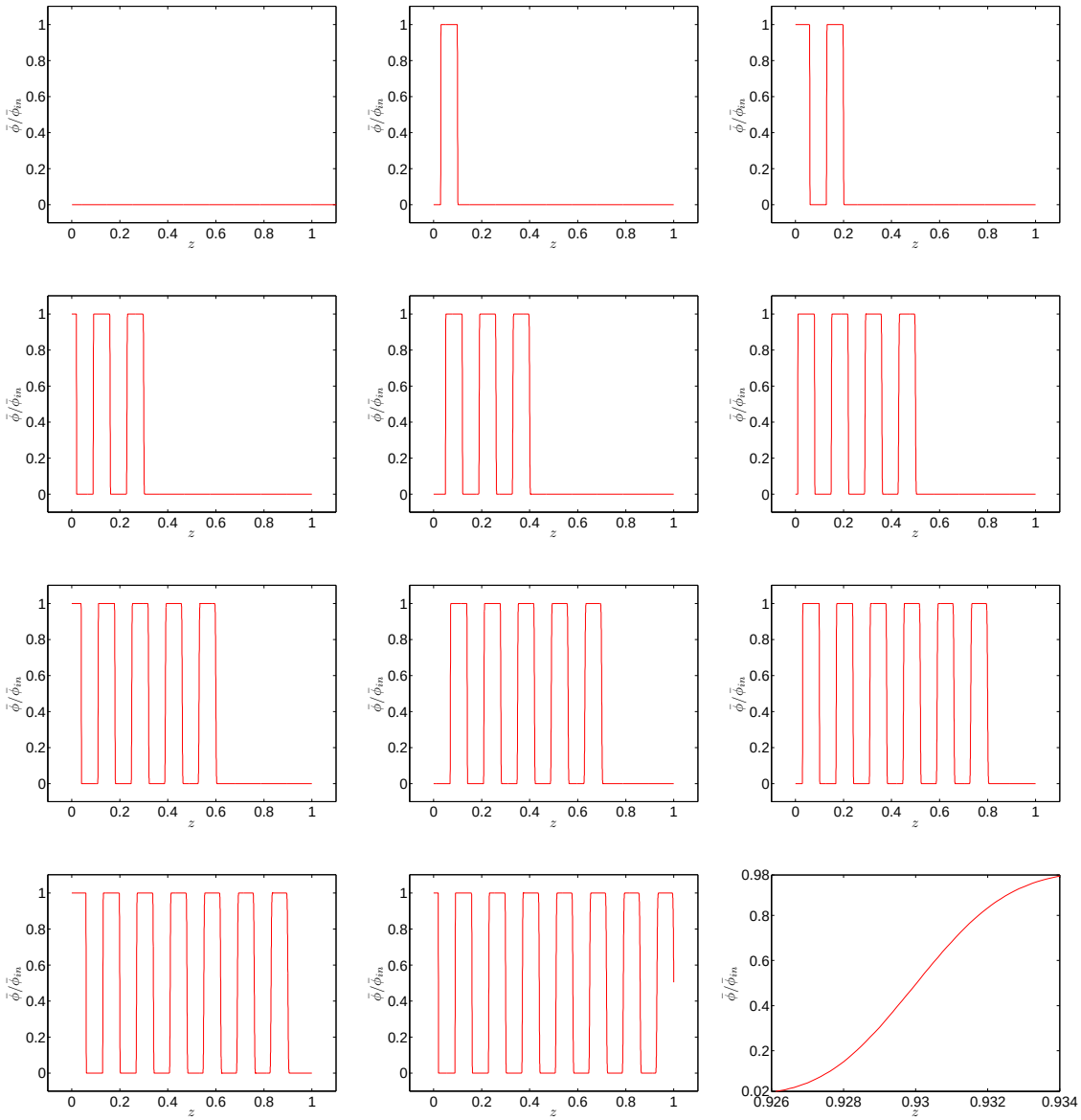

Figure 3.8: Results of solving (2.70) for a typical set of process parameters and a dimensionless time interval of 0.1 between pulses. The last figure shows the spreading of the last pulse (backward step), amplified in the axial coordinate. Here, we have $Re = 4318, B = 0, Fr = 17.52, s = 2.65, \delta = 2.067 \times 10^{-5}, \delta_p = 0.009, \bar{\phi}_{in} = 30\%, n = 0.5$.

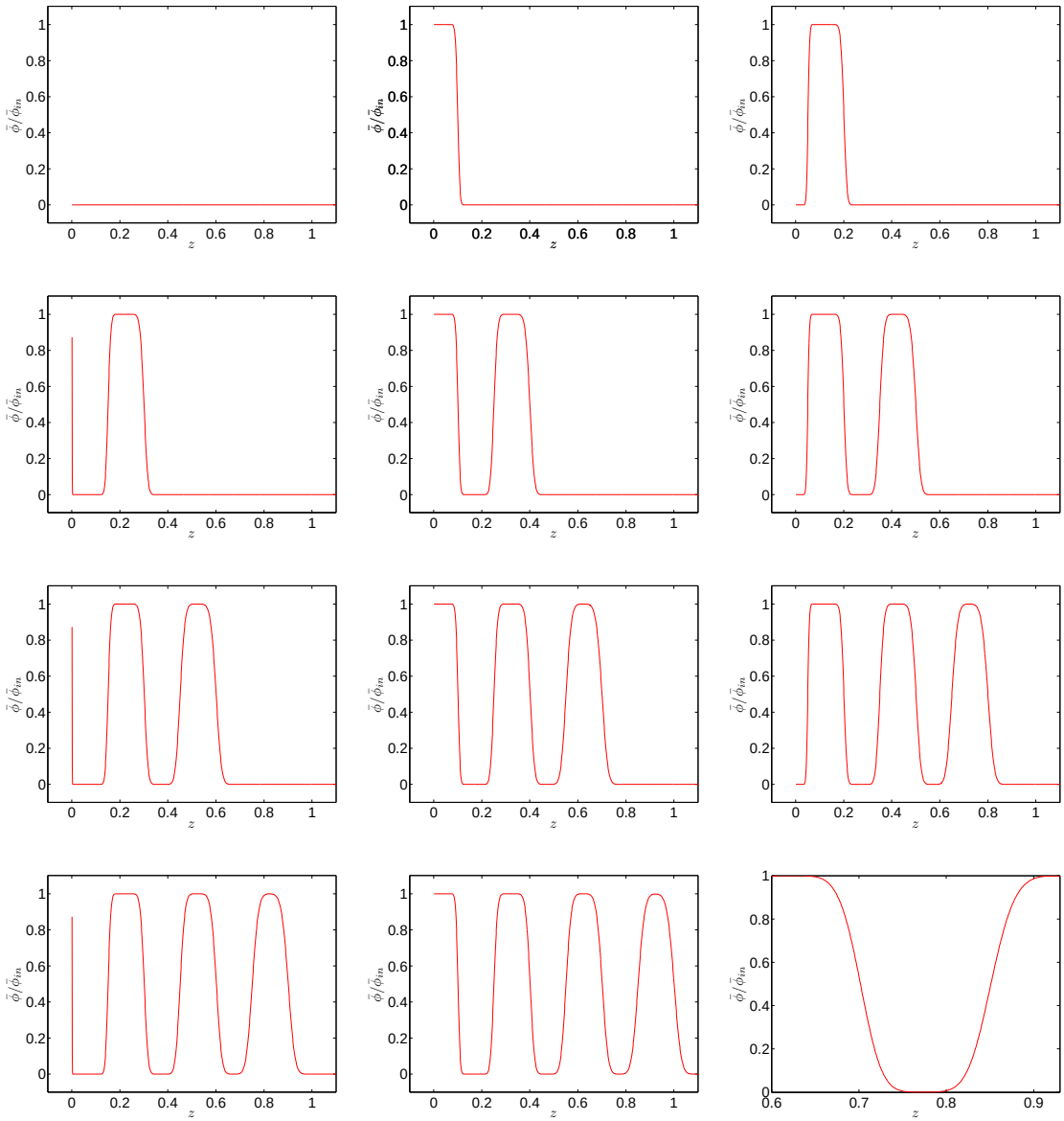

Figure 3.9: Result of a typical example with $Re = 31000$, $B = 0.31$, $Fr = 10$, $s = 2.65$, $\delta = 0.001$, $\delta_p = 0.01$, $\bar{\phi}_{in} = 30\%$, $n = 1$ and pulsation timescale 0.15. The snapshots are shown with dimensionless time interval of 0.1. The last figure zooms at the last pulses and shows there is no interaction between pulses.

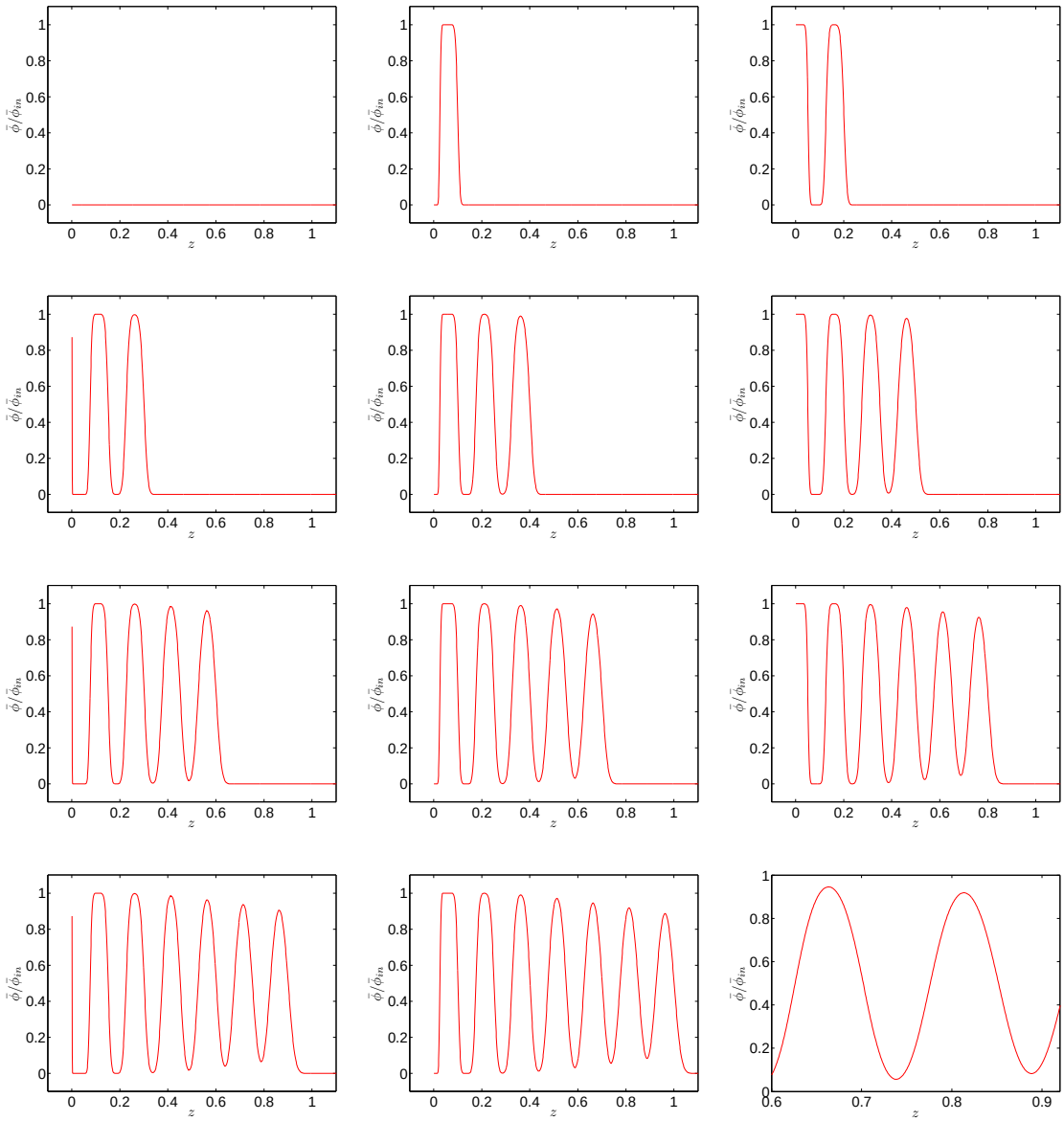

Figure 3.10: We double the number of pulses in previous example (see Fig. 3.9) which results in pulse interaction. The snapshots are shown with dimensionless time interval of 0.1. The last figure zooms at the last pulses and shows the interaction between pulses.

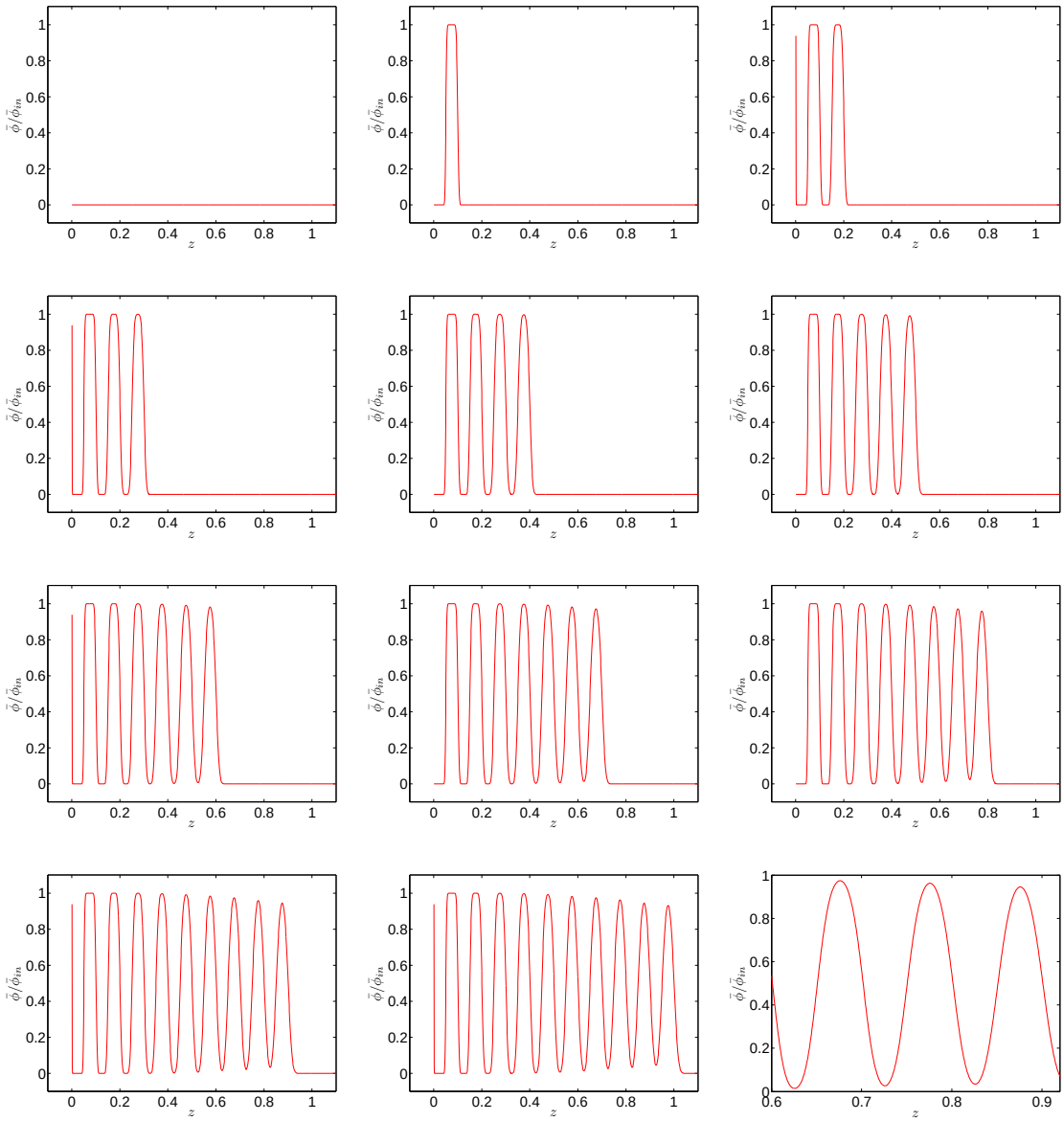

Figure 3.11: In this example the length of the pipe is 3 times longer than in example of Fig. 3.9. The snapshots are shown with dimensionless time interval of 0.1. The last figure zooms at the last pulses and shows the interaction between pulses.

Chapter 4

Summary

The work presented in this thesis has given a simple model to describe dispersion of a particulate slug in a vertical pipe, when the flow is turbulent and the fluid is shear-thinning with yield stress. This type of flow finds application in recent developments of hydraulic fracturing techniques.

In chapter 1, we give a brief introduction to fracturing flows and associated literature, then we continued with a crude consideration of the types of fracturing flow that occur within the pipe. This focuses on bulk flow characteristics and on what happen at a typical particle scale. In general, over the range of fully turbulent suspension flows likely to be observed, we can have flows that are both inertial and non-inertial on the particle scale, depending largely on the fracking fluid being pumped and on the flow rates. For those flows that are non-inertial on the micro-scale, an appropriate simplification would be to treat the slurry as a homogeneous single phase mixture. For higher shear flows and/or with less viscous fracking fluids the phases are only weakly coupled and are inertial at a local scale, as well as being fully turbulent in the bulk sense. For these flows, the suspension is still largely a homogeneous mixture, but a more sophisticated model is appropriate for describing particle-scale inertial effects. For both cases, we need to also deal with the non-Newtonian character of the fracking fluid in developing the model.

In chapter 2, we considered a model developed from the two-phase governing equations, assuming that solid and fluid phases can be described as two phases of incompressible continua. We simplified the governing equations to obtain a logarithmic approximation to the velocity profile for the mixture of solid and fluid. Also, closures for the slip velocity and friction factor were

obtained. We applied the method of multiple timescale to derive a transport equation for solid phase. This transport equation is a 1D advection-diffusion model for the leading order volume fraction of solid particles. The advection part includes the transport of solid phase with mean flow and particle settling. The diffusive part includes both the average diffusivity and Taylor dispersion. We evaluated the dispersion term for for 3 sensible particle diffusivity models. We showed that the Taylor dispersion effect generally dominates diffusivity and that the spreading of a solids front due to dispersion generally dominates advective spreading (rarefaction). Based on this model, we developed 2 estimates for the "mixing length" of a slug of proppant slurry pumped in a clear fracking fluid: due to settling of the particles (advection) and diffusion of the particles. We gave estimates of these mixing lengths for a wide range of flow parameters.

In chapter 3, we provided an accurate numerical algorithm for solution of the nonlinear 1D advection-diffusion model. Using this we showed how pulses of proppant may or may not interact for typical process parameters.

In general, we can summarize the significant novel contributions of this thesis as follows.

- The method of multiple timescale has been applied to derive a 1D advection/diffusion model for the leading order volume fraction of solid particles. The model includes both settling and dispersion effects.

- A robust numerical scheme has been developed and programmed to solve the nonlinear advection-diffusion equation for solid transport.

- 2 analytical mixing lengths estimates have been introduced (due to advection (settling) and diffusion of particles), in order to estimate the spreading of pulses more directly, i.e. suitable for field application.

Recommendations and future directions

The following areas appeared to show promise for future development.

- It is of practical interest to study wellbore inclination effects. In dealing with inclined and horizontal sections of well prior to the fracture, even small settling velocities become important. There are numerous criteria for predicting flow regimes in horizontal slurry transport, e.g. [44]. Although the vertical part of the pipe transport may be relatively uninfluenced by settling for many flows, the horizontal sections need designing to lie above the critical velocity for bed formation.

- In using particle diffusivity model of Eskin [17] and Walton [48], we implemented our own closure for friction factor, which might not be accurate. More clearly, the estimates of Taylor dispersion are wholly relate to the mean axial velocity profile, which are in turn coupled to the friction factor. Essentially, these should be applied together.

- Experimental, computational and theoretical techniques should be considered to improve the available closures for the drag coefficient, settling velocity, particle diffusivity and the constitutive laws for yield stress fluid suspensions.

Bibliography

[1] Bürger, R. Phenomenological foundation and mathematical theory of sedimentation-consolidation processes *Chemical Engineering Journal.* **80**, 177-188, (2000)

[2] Mahaut., F. Chateau, X., Coussot, P. and Ovarlez, G. Yield stress and elastic modulus of suspensions of noncolloidal particles in yield stress fluids. *J. Rheology.* **52**, 287-313, (2008)

[3] Chateau, X., Ovarlez, G., Luu Trung, K *Homogenization approach to the behavior of suspensions of noncolloidal particles in yield stress fluids.* J. Rheol. **52**, 489-506, (2008)

[4] P. Coussot and C. Ancey *Rheophysical classification of concentrated suspensions and granular pastes.* Phys. Rev. E **59**(4), 4445-4457, (1999)

[5] Coussot, P., Tocquer, L., Lanos, C., Ovarlez, G. *Macroscopic vs local rheology of yield stress fluids.* J. Non-Newt. Fluid Mech. **158**, 85-90, (2009)

[6] Crowe, C.T., Troutt, T.R. and Chung. J.N. Numerical models for two-phase turbulent flows. *Ann. Rev. Fluid Mech.* **28**, 11-43, (1996)

[7] Crowe, C.T. 2006 *Multiphase Flow Handbook* CRC Press

[8] Crowe., C.T, Schwarzkopf., J.D., Sommerfeld., M. and Tsuji.Y 2012 *Multiphase Flows with droplets and particles* CRC Press

[9] Crowe., C.T *On models for turbulence modulation in fluid-particle flows International Journal of Multiphase Flow* **26**, 719-727, (2000)

[10] Drew, D. A. Mathematical modeling of two-phase flow. *Ann. Rev. Fluid Mech.* **15**, 261-291, (1983)

[11] dḾuteau, E., Gillard, M., Miller, M., Pena, A., Johnson, J., Turner, M., Medvedev, O., Rhein, T., & Willberg, D. *Open-Channel Fracturing A Fast Track to Production* Oilfield Review Autumn, pp. 4-17, (2011)

[12] Dougherty, T.J. 1959 Some problems in the theory of colloids. PhD Thesis, Case Institute of Technology.

[13] Drew, D. A. Mathematical modeling of two-phase flow. *Ann. Rev. Fluid Mech.* **15**, 261-291, (1983)

[14] Eskin, D., Leonenko, Y., Vinogradov, O. On a turbulence model for slurry flow in pipelines. Chem. Eng. Sci. 59, 557-565, (2004)

[15] Eskin, D., An engineering model of solids diffusivity in hydraulic conveying Powder Technology 159, 78-86, (2005)

[16] Eskin, D., Miller, M.J., A model of non-Newtonian slurry flow in a fracture Powder Technology 182, 313-322, (2008)

[17] Eskin, D., A simple model of particle diffusivity in horizontal hydrotransport pipelines Chem. Eng. Sci. 82, 84-94, (2012)

[18] Frigaard, I.A. *Dispersion of solids in fracturing flows: strategic modeling review.* Confidential consulting report prepared for Schlumberger NTC, April 2013.

[19] Hammond, P.S. *Settling and slumping in a Newtonian slurry, and implications for proppant placement during hydraulic fracturing of gas wells.* Chem. Eng. Sci. **50**, pp. 3247-3260, (1995)

[20] Ishii, M. and Hibiki.T 2011 *Thermo-fluid dynamics of two-phase flow* Springer.

[21] Krieger, I.M., Rheology of monodisperse lattices. Adv. Coll. Int. Sci. 3, 111-136, (1972)

[22] Lakhtychkin, A., Vinogradov, O., Eskin, D. *Modeling of Placement of Immiscible Fluids of Different Rheology into a Hydraulic Fracture* Ind. Eng. Chem. Res. **50**, pp. 5774-5782, (2011)

[23] Leveque, R.J 2002 *Finite volume methods for hyperbolic problems* Cambridge texts in applied mathematics.

[24] Chateau, X., Ovarlez, G. and Trung, K.L. Homogenization approach to the behavior of suspensions of noncolloidal particles in yield stress fluids. *J. Rheology.* **52**, 489-506, (2008)

[25] Meek, P.C., Norbury, J. *Two-stage, two-model finite difference schemes for non-linear parabolic equations.* IMA. J.Num.Analysis **2**, 335-356, (1982)

[26] Mahaut, F., Chateau, X., Coussot, P., Ovarlez, G. *Yield stress and elastic modulus of suspensions of noncolloidal particles in yield stress fluids.* J. Rheol. **52**, 287-313, (2008)

[27] Maron, SH, Pierce, PE, 1956 J Colloid Sci 11, 80-95

[28] Mobbs A.T., Hammond, P.S. *Computer Simulations of Proppant Transport in a Hydraulic Fracture* SPE Production & Facilities, May 2001, pp. 112-121, (2001); SPE paper 69212.

[29] Nessyahu, H., Tadmor, E. *Non-oscillatory central differencing for hyperbolic conservation laws.* J. Comput.Phys. **87**, 408, (1990)

[30] Oroskar, A.R., Turian, R.M. The critical velocity in Pipeline flow of slurries. *AIChE.* **26**, 550, (1980)

[31] Ovarlez, G., Bertrand, F., Rodts, S. *Local determination of the constitutive law of a dense suspension of noncolloidal particles through MRI.* J. Rheol. **50**, 259-292, (2006)

[32] Ovarlez, G., Bertrand, F., Coussot, P., Chateau, X. *Shear-induced sedimentation in yield stress fluids.* J. Non-Newt. Fluid Mech. **177-178**, 19-28, (2012)

[33] Pearson, J.R.A. *On suspension transport in a fracture: framework for a global model.* J. Non-Newt. Fluid Mech. **54**, pp. 503-513, (1994)

[34] Quemada, D. (1982) Lecture Notes in Physics, 164: Casas-Vazquez J, Lebon J (eds), Stability of Thermodynamic Systems, pp 210-247, Springer, Berlin

[35] M.C. Roco and C.A. Schook *Modelling of slurry flow: the effect of particle size.* Can. J. Chem. Eng., **61**, pp. 494–503, (1983)

[36] J.F. Richardson and W.N. Zaki *Sedimentation and fluidisation: Part 1.* Trans. Inst. Chem. Eng., **32**, pp. 35-53, (1954)

[37] M.C. Roco and C.A. Schook *A modelling for turbulent slurry flow.* J. Pipelines, **4**, pp. 3–13, (1984)

[38] Rudman., M. Blackburn, H.M., Graham, L.J.W., Pullum, L. Turbulent pipe flow of shear-thinning fluids *J. Non-Newt. Fluid Mech.* **118**(1), 33-48, (2004)

[39] Samir, M. *Novel Technique to Increase Production from Tight Reservoirs using Channel Fracturing Technique for the first time in the Middle East and North Africa* SPE Sahara Oil & Gas Company, April 2013, pp. 1-10; SPE paper 164655.

[40] Samir, M., Kamal, M., Mathur, A., Semary, M., Yosry, M., Bernechea, J.M., Kamar, A. & Mokhtar, A. *Production Enhancement in the Egyptian Western Desert using the Channel Fracturing Technique A Field Case Study* SPE Sahara Oil & Gas Company, April 2013, pp. 1-10; SPE paper 164709.

[41] Tabuteau H, Coussot P, de Bruyn JR. Drag force on a sphere in steady motion through a yield-stress fluid. *J. Rheol.* 51:125-37, (2007)

[42] Taylor, G. The dispersion of matter in turbulent flow through a pipe. *Proceedings of the Royal Society of London. Series A. Mathematical and Physical Sciences* **223** (1155), 446-468, (1954)

[43] Tennekes, H. and Lumley.J.L 1972 *A First Course in Turbulence* MIT press.

[44] Turian., R.M., Yuan, T.-F. *Flow of slurries in pipelines* AIChE Journal, **23**(3), 232-243, (1977)

[45] Truesdell, C. 1984 *Rational thermodynamics* Springer-Verlag, New York-Berlin-Heidelberg.

[46] Valco, P. and Economides.M. J 1995 *Hydraulic Fracture Mechanics* JOHN WILEY & SONS.

[47] Vu, T.S., Ovarlez, G., Chateau, X. *Macroscopic behavior of bidisperse suspensions of noncolloidal particles in yield stress fluids.* J. Rheol. **54**, 815–833, (2010)

[48] Walton I. C. Eddy diffusivity of solid particles in a turbulent liquid flow in a horizantal pipe. *AIChE.* **41**(7), 1815-1820, (1995)

[49] Wierenga, A.M., Philips, A.P., Low-shear viscosity of isotropic dispersions of (Brownian) rods and fibres; a review of theory and experiments. Coll. Surf. A, 137, 355-372, (1998)